

THESIS FOR THE DEGREE OF LICENTIATE OF PHILOSOPHY

Quantitative Transmission Electron Microscopy Studies of  
the Porous Structure of Silica Nanoparticle Gels

CHARLOTTE HAMNGREN BLOMQVIST



Department of Applied Physics  
CHALMERS UNIVERSITY OF TECHNOLOGY  
Gothenburg, Sweden 2015

Quantitative Transmission Electron Microscopy Studies of the Porous Structure of Silica Nanoparticle Gels

CHARLOTTE HAMNGREN BLOMQVIST

© Charlotte Hamngren Blomqvist, 2015

Cover image:

**Left:** Transmission electron micrograph of dried silica nanoparticles with a nominal particle diameter of 20 nm. **Upper center:** Transmission electron micrograph of a silica nanoparticle gel with a nominal particle diameter of 5.0 nm. **Lower center:** 3D reconstructions of two different silica gel samples, the upper sample has a nominal particle diameter of 20 nm, and the lower sample has a nominal particle diameter of 5.0 nm. **Right:** Flow lines through the 5.0 nm particle gel, simulated using the Lattice-Boltzmann method. Image courtesy of Tobias Gebäck.

Department of Applied Physics  
Chalmers University of Technology, SE-412 96 Göteborg  
Tel: +46 (0)31-7721000  
<http://www.chalmers.se/ap/EN>

Printed by Chalmers Reproservice,  
Gothenburg, Sweden 2015

# Quantitative Transmission Electron Microscopy Studies of the Porous Structure of Silica Nanoparticle Gels

CHARLOTTE HAMNGREN BLOMQVIST

Department of Applied Physics  
Chalmers University of Technology

## Abstract

The flow and diffusion through porous structures are strongly influenced by pore size distributions, pore connectivity and structure of the pore walls. In one of the included articles, the connection between pore sizes and water transport on different length scales was investigated. For an even deeper understanding of the correlation between structure and transport, more information about the 3D structure is needed. Hence, we have used both electron tomography for direct measurements of the 3D structure, and a statistical method for going from 2D to 3D by computer simulations.

We experimentally show that for a pore size of less than 120 nm, the pore size distribution has little or no impact on the water permeability. We also present an approach for estimating the 3D structure from 2D images, using the intensity profile as a structure parameter in the third dimension. The next step in the ongoing research is direct 3D imaging of the samples.

The study was conducted by characterising silica nanoparticle gels in both 2D and 3D. The 2D structure data were obtained by transmission electron microscopy (TEM) and high-angle annular dark-field scanning transmission electron microscopy (HAADF-STEM). Statistical and geometrical image analysis methods were used for the data analysis. The 3D data were acquired using HAADF-STEM tomography.

The experimental studies of transport involved flow measurements and nuclear magnetic resonance imaging (NMR) diffusometry. The computational part included Lattice Boltzmann (LB) simulations of flow and diffusion through the reconstructed 3D structure of the sample.

This work contributes to the field of water transport through soft porous materials, adding experimental direct observations of the porous structure on the 3D nanoscale. This information is highly relevant when developing an understanding for the correlation between structural properties and mass transport. The development of porous materials with specific mass transport properties relies on this detailed knowledge. The work has impact on several fields of research and development, e.g. pharmaceuticals, catalysts, hygiene products, food and batteries.

---

**Keywords:** Soft matter, silica gel, 3D (s)TEM, nanoporous, mass transport, liquid permeability.



*A line is made up of points as is a string of beads; a plane is made up of lines as is a cloth of threads; a solid is made up of planes as is a book of pages.*

- B. Cavalieri (1598 - 1647)

# PREFACE

The research presented in this thesis was carried out at the Division for Microscopy and Microanalysis and in the Eva Olsson group, at the Department of Applied Physics, Chalmers University of Technology, Göteborg, Sweden, between February 2011 and March 2015. The project is a part of the VINN EXCELLENCE centre Supramolecular Biomaterials (SuMo), and the work was conducted with supervision of Prof. Eva Olsson and Prof. Anne-Marie Hermansson, assistant supervisors Dr. Stefan Gustafsson and Adj. Prof. Niklas Lorén, and mentor Annika Altskär.

Göteborg, 18th March 2015  
*Charlotte Hamngren Blomqvist*

## LIST OF PUBLICATIONS

This thesis is based on, but not limited to, the work contained in the following scientific papers, referred to by their Roman numerals in the text:

### **I Pore Size Effects on Convective Flow and Diffusion Through Nanoporous Silica Gels**

**C. Hamngren Blomqvist**, C. Abrahamsson, T. Gebäck, A. Altskär, A.-M. Hermansson, M. Nydén, S. Gustafsson, N. Lorén, and E. Olsson.

*In manuscript (2015).*

### **II Estimation of Mass Thickness Response of Embedded Aggregated Silica Nanospheres from High Angle Annular Dark-Field Scanning Transmission Electron Micrographs**

M. Nordin, C. Abrahamsson, **C. Hamngren Blomqvist**, H. Häbel, M. Röding, E. Olsson, M. Nydén, and M. Rudemo.

Journal of Microscopy, **253**, (2), 166-170, (2014).

## CONTRIBUTION REPORT

**Paper I.** I made and prepared the samples, performed the STEM/TEM imaging in 2D and 3D, and performed the stereological image analysis. I wrote the paper.

**Paper II.** I performed the HAADF-STEM imaging, the detector radius measurements and the thin sectioning of the sample. I wrote the Material and methods parts on plastic embedding and ultramicrotome sectioning.

## RELATED PUBLICATIONS NOT INCLUDED IN THE THESIS

- **From Static Micrographs to Particle Aggregation Dynamics in Three Dimensions**

H. Häbel, A. Särkkä, M. Rudemo, **C. Hamngren Blomqvist**, E. Olsson, C. Abrahamsson, and M. Nordin.

*In manuscript (2015).*

## LIST OF ABBREVIATIONS

2D	Two-dimensional or two dimensions
3D	Three-dimensional or three dimensions
3D TEM	Transmission electron microscope tomography
3D STEM	Scanning transmission electron microscope tomography
AMD	Arithmetic mean diameter
BF	Bright field
CCD	Charge-coupled device
FEG	Field emission gun
HAADF	High-angular annular dark field
ISA	Intrinsic surface area
LB	Lattice-Boltzmann
MW	Missing wedge
NMR	Nuclear magnetic resonance
PSD	Pore size distribution
SIRT	Simultaneous iterative reconstruction technique
STEM	Scanning transmission electron microscope/y
TEM	Transmission electron microscope/y
VWMV	Volume-weighted mean volume
WBP	Weighted back projection

# Contents

<b>1</b>	<b>Introduction</b>	<b>1</b>
1.1	Soft porous materials and gels . . . . .	1
1.2	Mass transport in gels . . . . .	2
1.3	Silica nanoparticle gels . . . . .	4
1.4	Scientific challenges of nanoscale imaging of soft porous materials . .	5
1.5	Scope of work . . . . .	6
<b>2</b>	<b>Materials and methods</b>	<b>7</b>
2.1	Gel fabrication . . . . .	7
2.2	Dehydration, infiltration and embedding . . . . .	8
2.3	Ultramicrotome thin sectioning . . . . .	9
2.4	Freeze fracture and freeze etching . . . . .	11
2.5	TEM and STEM contrast mechanisms and equipment . . . . .	11
2.6	Statistical analysis models . . . . .	20
2.7	Mass transport measurements . . . . .	22
<b>3</b>	<b>Results and discussion</b>	<b>25</b>
3.1	Ensuring an appropriate sample preparation method . . . . .	25
3.2	Sample selection based on porous length scale . . . . .	26
3.3	Pore size effects on flow and diffusion through nanoporous silica gels .	27
3.4	Estimation of mass thickness of embedded aggregated silica nanospheres	32
3.5	Ongoing study: 3D imaging of nanostructured silica gels . . . . .	33
<b>4</b>	<b>Summary of included papers</b>	<b>37</b>
4.1	<b>Paper I</b> . . . . .	37
4.2	<b>Paper II</b> . . . . .	37
<b>5</b>	<b>Summary of work</b>	<b>39</b>
5.1	Conclusions . . . . .	39
5.2	Outlook . . . . .	40
	<b>Bibliography</b>	<b>45</b>
	<b>Papers I–II</b>	



## Chapter 1

# Introduction

### 1.1 Soft porous materials and gels

As stated by Pierre-Gilles de Gennes in his Nobel lecture in 1991[1], soft matter (earlier called "complex fluids") is highly flexible, in the sense that its mechanical properties can be easily influenced by minor chemical, thermal or mechanical actions (e.g. shearing). The molecules forming the soft materials are on a length scale in-between atomic sizes and the microscopic scale, and they often interact via weak physical bonds. The formation of soft materials is to a large extent influenced by the fluctuations and Brownian motions of the molecules within the material. Since soft materials can have both hydrophilic and hydrophobic domains, the formation of self-assembled and hierarchical structures are very common[2].

Despite a rapid development of the soft material research field, a common definition is not yet specified. However, the scientific journal *Soft Matter* states that the area of soft materials includes, but is not limited to: gels, polymers, colloids, vesicles, emulsions, films, surfactants, micelles, suspensions, liquid crystals, biological macromolecules, membranes, biocomposites and biomimetic materials[3]. Soft porous materials are used in or as a part of different kinds of everyday products and applications, e.g. food and pharmaceuticals[4], chromatographic gels[5], catalysts[6, 7], hygiene products and batteries[8].

Soft, water containing, porous materials are studied in this work. The term porous materials spans from materials with only closed pores (voids), to materials where all voids are interconnected. The porous network can have a varying pore diameter and multiple branches. The details of the structure of the pores, including size and morphology, have a large impact on the transport of liquids through the material[9]. This determines the performance of soft materials in many of the applications mentioned above.

Gel structures constitute one important subcategory of soft materials. A common definition of a gel is a material composed of microscopic subunits (e.g. nanoparticles or polymer subunits) which bind to each other, forming a continuous 3D network on the macroscopic scale. Formation of this network is usually described by the

percolation model. When the percolated system spans the entire available volume, the gel point is reached and the material properties changes abruptly. Gel definitions differ for chemical and physical gels: chemical gels have subunits that are covalently linked, and physical gels are held together by physical interactions. Physical gels can for example be thermoreversible[2]. Gels are structurally disordered, and can display both solid and liquid-like properties. They can also contain a large proportion of liquid solvent (e.g. water)[2].

Pore sizes in porous materials are traditionally investigated using different indirect methods[10–18], e.g. liquid intrusion or adsorption techniques, calorimetric methods or X-ray scattering techniques. A more direct method of studying the pores is by determining and reconstructing the 3D details of the porous structure. This approach provides a better understanding of the pore connectivity and morphology within the material.

## 1.2 Mass transport in gels

A common denominator for the applications of soft porous materials is the desire to control the mass transport (i.e. flow and diffusion) through the material. The material transport properties for water (or other fluids, molecules or particles) are to a large extent determined by the structure of the material, ranging from the molecular scale to the macroscopic scale. The properties of the transported molecules are also very important factors influencing the mass transport. For example, the ratio between the molecule size and the mesh size of the porous network has a large impact on the fluid transport. Other molecule parameters affecting the transport can be i.e. molecular weight, flexibility, charge and shape. Another material property affecting the mass transport is the surface chemistry of the pores, for example the hydrophobicity or hydrophilicity of the surfaces. In order to describe how a fluid finds its way through the 3D porous structure, structure information from only 2D images is generally not enough, regardless of whether the image represents a projection of the 3D structure or a planar cut through it. This is due to the molecules of the fluid travelling through the material along paths (i.e. the pores) which span all three spatial dimensions.

Previous works have shown a strong correlation between mass transport and structure[4, 10, 19–21]. Hermansson and Lucisano[22], and Hermansson[9, 23, 24] showed how different parameters during gel fabrication (e.g. pH, temperature and ionic strength) can influence the water handling properties of different protein gels, due to changes in the gel morphology. The studies show that materials with pore sizes in the range from approximately 200 nm and up to 2  $\mu\text{m}$  are more predisposed to lose moisture, compared to materials structured on a smaller scale[9].

In 2013, Sott et al.[25] developed a generic methodology for studying flow with micro-particle image velocimetry in soft materials. A model porous structure, patterned in poly(dimethylsiloxane) mimicked the porous structure of  $\beta$ -lactoglobuline

gels retrieved by confocal microscopy. Experimental results were compared to flow simulations. It was concluded that the results and simulations, indeed show that the detailed microstructure is important for the mass transport characteristics of a material. Abrahamsson et al.[26] studied diffusion and gravitationally driven flow in porous mixed clay gels, where colloidal silica nanoparticles were used as a supporting structure. Both studies involved materials with pores larger than 100 nm. Hence, porous networks with length scales smaller than 100 nm have not previously been experimentally studied with respect to nanoscale morphology effects on flow and diffusion.

It is known that flow is dominating over diffusion on the larger length scale, and vice versa (assuming that the applied pressure is not changed). Also, the importance of diffusion is expected to increase rapidly with decreasing pore radius. The transition region between flow and diffusion is not yet well understood in nanostructured materials. It is therefore of utmost importance to determine the correlation between structure and transport properties in order to improve and design new materials with tailored properties[4, 26–28]. This relationship has not earlier been studied on the nanoscale using methods taking the 3D structure and morphology of the pores into account.

### 1.2.1 Flow

When a fluid or particles are transported along a gradient, e.g. a pressure gradient or a gravitational gradient, it is referred to as flow. In this work, the flow through the porous material is driven by a pressure gradient.

The Hagen-Poiseuille relationship,

$$Q = \frac{\pi R^4}{8L\eta} p, \quad (1.1)$$

is used for determining how well a pipe transports fluid. In this relationship, the pores are assumed straight, and the flow is steady and laminar. The flow rate ( $Q$ ) is proportional to the pipe radius to the power of four ( $R^4$ ), and inversely proportional to the pipe length ( $L$ ). As a consequence, for a specific pressure, the flow rate through larger pores will be much higher than for smaller pores. Thus, the importance of flow as the dominating mass transport mechanism is expected to decrease with decreasing pore radius.  $\eta$  denotes the fluid viscosity, and  $p$  is the pressure drop, driving the flow. In comparison with Ohm's law the pressure drop is equivalent to the potential drop, which drives a current. According to the same analogy, the (hydrodynamic) resistance of the pipe is given by  $\frac{8\eta L}{\pi R^4}$ [29].

The Reynold's number (Re) is a dimensionless ratio between inertial and frictional forces in a flow, and is used for characterising a flow as laminar or turbulent. It is defined as

$$\text{Re} = \frac{\mathbf{F}_{inertial}}{\mathbf{F}_{viscous}} = \rho \frac{vl}{\eta}, \quad (1.2)$$

where  $\rho$  and  $\eta$  represents the density and viscosity of the fluid respectively, and  $v$  and  $l$  denotes the characteristic velocities and length scales of the investigated system respectively[29]. In order for turbulent flows to occur, the Re is generally less than 2300[30].

### 1.2.2 Diffusion

Diffusion originates from the concept of Brownian motion of molecules. It is a random motion driven by the internal heat of the system. Diffusion is often discussed in terms of molecules having a net movement along a concentration gradient according to the second law of thermodynamics. Eventually the gradient will fade away, but the local movement of the individual molecule is not affected. If only one type of molecule is present, the diffusion is often referred to as self-diffusion, as is the case in this work.

The interactions between the fluid and the solid network structure is very rapid, and the diffusion properties are determined by a variety of factors. There is still no unified theory predicting the particle movements in all categories of structures, instead there are several models, all optimised for certain type of system. Factors affecting the diffusion are for example the obstruction by the solid network structure, the hydrodynamic and the thermodynamic interactions (e.g. pore discontinuities or interface interactions)[31]. Hence, both the surface area and the accessible volume fraction are important factors influencing the diffusion properties.

A useful quantity for evaluating the length scale in relation to flow and diffusion is the Peclét number (Pe). It is defined as

$$\text{Pe} = \frac{vd}{D}, \quad (1.3)$$

where  $v$  can denote the flow speed through the material,  $d$  denotes the characteristic length scale or length of the system, and  $D$  is the diffusion coefficient of the medium (within the porous sample). If the Pe number is larger than one, flow is dominating, and if it is smaller than one, diffusion is dominating[29]. In this work, we investigate systems where the Pe number is close to one.

## 1.3 Silica nanoparticle gels

Amorphous silicone dioxide ( $\text{SiO}_2$ ), also known as silica, is the most common compound of the Earth's crust[32]. Colloidal silica gels are chemical gels, and can be described as sols of colloidal amorphous silica nanoparticles that have undergone a process of gelation. During gelation, the silica particles agglomerate into a continuous network that spans the available volume[33]. This is a fractal process resulting in a particulate and fibrous structure. The silica interface to the water is naturally hydrophilic, but can be chemically modified if desired. The amorphous nanoparticles are covalently (i.e. irreversibly) bound to each other at the spatial point of

contact[32]. Silica gels are capable of containing very large fractions of water, and can for example be used together with a gelling agent for ground consolidation of building sites[34, 35], or as a gelled electrolyte in valve-regulated lead-acid (VRLA) batteries[8],[36]. The first transmission electron microscope (TEM) images of a silica gel were presented on the third international conference of electron microscopy in London, 1954[37].

Silica gels are highly relevant and useful systems for the study of e.g. mass transport and water management. With regards to the micro- and nanostructure of the gel, there are several tuneable structural parameters, for example surface area and solid volume fraction. There are also fabrication parameters: e.g. particle size and morphology, pH and ionic strength. Silica gels can thus be produced with small or large pore size distribution (PSD)s, with pores ranging from a few nanometres up to several micrometres. Since silica provides a distinctive contrast compared to the embedding resin both using TEM and scanning transmission electron microscopy (STEM), without the need of staining in order to further enhance the contrast between the particles and the surrounding medium. From these perspectives it is well suited for electron microscopy studies.

The mechanical and rheological properties of forming colloidal silica nanoparticles gels (e.g. gelation time, gel strength and elastic modulus) have been thoroughly investigated as a function of ionic strength and solid volume fraction[32, 38–40]. However, the focus has been on the aggregation process during gelation, as a function of ionic strength and silica concentration, rather than the actual structure of the finished gel.

## **1.4 Scientific challenges of nanoscale imaging of soft porous materials**

The analysis and handling of soft materials include many challenges. The materials often contain water, making them sensitive to e.g. heat, radiation and mechanical strain or stress. The vacuum within a traditional electron microscope specimen chamber causes evaporation of the water within the structure. This affects the sample structure and might even destroy it completely. This phenomenon calls for careful sample preparation where the liquid phase is either removed or solidified, e.g. by solvent exchange (plastic embedding), freeze etching or other cryogenic techniques.

Conventional TEM imaging creates only a 2D projection of the 3D material, where important information concerning actual size of the pores, pore connectivity and shape of connecting features, are not directly accessible. This means that a full characterisation of the transport paths, as well as the distribution and sizes of pores is not possible using only data from 2D imaging.

## 1.5 Scope of work

The main motivation for this work is to establish a more detailed knowledge about the porous structure of 3D soft porous materials. The work is focused on the study of the direct correlation between authentic quantitative structural data and mass transport properties on the nanometer scale of colloidal silica nanoparticle gels.

High resolution pore size analysis and material characterisation in 2D and 3D by TEM, STEM, transmission electron microscope tomography (3D TEM) and scanning 3D TEM (3D STEM) have been used for material characterisation. These direct methods of determining material structure, combined with image analysis and mass transport measurements, were the main techniques used for this work. Samples with a typical pore width representing the interval just below, in, and above the transition region between mass transport dominated by flow or diffusion were chosen.

Determination of the material structure in detail enabled the quantification of gel PSD, down to a few nanometres and facilitated analysis of the immediate connection between nanostructure and mass transport properties. A 3D characterisation of the structure would also provide a better understanding of the pore connectivity within the material. These reconstructions can be used as templates for simulating flow through the material.

The following list states the main research questions included in this licentiate work.

- How can the building blocks of the investigated silica gels be characterised?
- How does pore sizes and PSD in silica gels affect mass transport?
- Can a statistical approach enable the determination of the 3D structure from a 2D micrograph?
- How can the material structure be described in 3D?

## Chapter 2

# Materials and methods

Silica nanoparticle gels with different particle size and morphology were studied in this work. The nanoparticle silica gels were prepared from colloidal silica particle sols, and the samples were chosen for a more detailed study. Surface titration studies performed on these samples provided information about the nominal sizes for the silica spheres in the different sols. The diameters were 20 nm, 5.0 nm, and 3.6 nm, respectively[41].

Aggregation of silica nanoparticles occurs spontaneously if the particles are uncharged. Hence, the sols always contains charged particles. The decharging of the particle surfaces can be initiated by changes in pH, ionic strength or both, which initialises the gelation process. The formation of the silica network starts with the formation of reversible siloxane bonds (Si-O-Si) between nanoparticles in contact. After this initial bonding, there will be an almost infinitely small negative radius of curvature between the particles. At this location, the solubility of silica is zero. Hence, silica residue from the solution initiates the neck-formation at the binding sites, making the adjacent particles merge together seamlessly[32].

In order to investigate the nanostructure of the material, a number of different methods were needed. They are introduced and motivated in this chapter:

- Sample fabrication and preparation
- Specimen preparation for electron microscopy
- Data collection and image analysis using transmission electron microscopy
- Reconstruction and visualisation

## 2.1 Gel fabrication

The gel samples were prepared by lowering the pH of colloidal silica suspensions (kindly provided AkzoNobel Pulp and Performance Chemicals AB) by ion exchange (Dowex Marathon C, Sigma-Aldrich Co. LLC, Saint Louis, MO, USA) and addition

of NaCl. The ion exchange pearls were removed by suction filtration after use. Ultra-pure deionized water and NaCl were added to the filtered sols, adjusting the silica concentration from 42.3 wt% (Bindzil 40/130) and 15 wt% (Bindzil XP1 and GB3000), to 9.0 wt% for all samples. The GB3000 solution was doped with 0.4 wt% Bindzil 40/130. The next step was adjusting the NaCl concentration to the desired values for the different gels. Samples were immediately shaken in a vortex shaker and left to gel for one day (see figure 2.1a). Hereafter, the gels formed using Bindzil 40/130 (with a NaCl concentration of 0.5 M), XP1 and GB3000 (both with a NaCl concentration of 0.9 M), will be denoted as Gel 1, 2 and 3, respectively.

According to Mie theory, structures of a comparable size to visible light will scatter more as function of diameter of the scattering object[42]. In this case the "scattering object" applies to the pores, since they are of a comparable size as the wavelength of visible light. The same phenomenon has been confirmed for several porous structures, e.g. in amelogenin gels[43]. These scattering differences are present in colloidal silica gels, and can clearly be seen in figure 2.1b, confirming the statement above. Here, Gel 1 has the coarsest pore network (both in pore size and particle size) and Gel 3 has the finest network.



**Figure 2.1:** (a) The gel samples were prepared in glass vials with a diameter of 24 mm. A scalpel was used for cutting  $1 \times 1 \times 1 \text{ mm}^3$  gel samples for plastic embedding. Samples were retrieved from the bulk part of the gel, where no surface effects were likely to occur. (b) The three different gel samples, here contained in NMR tubes. Large differences in opacity can be seen. From top to bottom, the sample order is: Gel 1, 2 and 3.

## 2.2 Dehydration, infiltration and embedding

In order to prepare specimens for TEM and STEM, the water had to be carefully removed. Pieces that were approximately  $1 \times 1 \times 1 \text{ mm}^3$  were isolated from the inner volume of the gel sample, and subsequently infiltrated with a resin (TLV, TAAB laboratories, England). The infiltration technique, using a low-viscosity resin, is based on the commonly<sup>1</sup> used technique originally presented by Spurr[44]. The

<sup>1</sup>Approximately 12,900 citations (*Web of Science, January 3, 2015*).

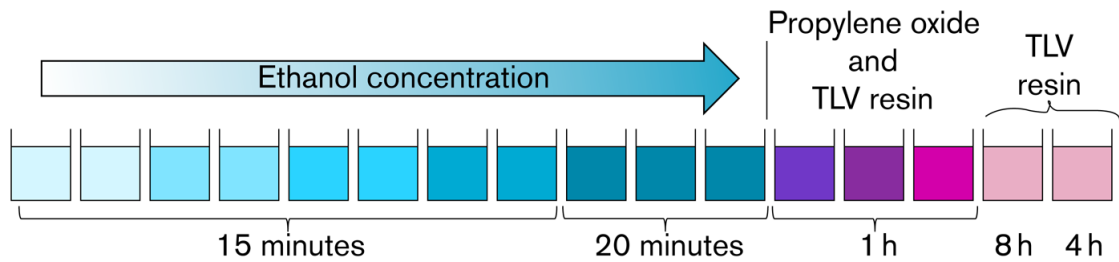


**Figure 2.2:** Schematic representation of the plastic embedding process. The samples were embedded in resin by dehydration in a graded series of ethanol, propylene oxide and resin. In an automated carousel, the gel cubes were subsequently treated with each of eleven solutions of ethanol (ranging from 30% to 99.5%) followed by two submersions in 100% propylene oxide, and two steps of ascending resin concentrations up to the last step of pure resin. The NaCl concentration in the ethanol solutions was kept at the same level as in the respective gels for ethanol concentrations of up to 70%.

resin has been developed further, and the infiltration technique is now standard procedure[45].

As a first step of the infiltration process, the gel pieces were dehydrated in an ascending series of ethanol up to 99.5%, followed by a propylene oxide treatment, and finally a graded resin series of preparations up to pure resin (see figure 2.2). A gradually increasing ethanol concentration was used in order to prevent sample shrinkage. In case of a small amount of shrinkage, it is assumed to be isotropic[28]. Any shrinkage would have presented itself already after the infiltration process, and no such indications were detected for the silica gels.

After the solvent exchange, the silica cubes were embedded in plastic blocks of  $10 \times 5 \times 5 \text{ mm}^3$ , for easier handling during the sectioning process. A large challenge during sectioning was the fact that both the silica blocks and the embedding plastic were more or less clear and transparent, making the silica difficult to locate within the block. This was solved by covering the silica cube in talcum powder immediately prior to the embedding. The talcum made it easier to locate the edges of the silica cube within the plastic block.

## 2.3 Ultramicrotome thin sectioning

Thin sections of between 70 nm and 300 nm were generated using a PowerTome XL (RMC products, Boeckeler Instruments Inc., Tucson, Arizona) and a diamond knife (DiATOME, Biel, Switzerland), see figure 2.3. The sections were placed on 200-mesh carbon support film Cu-grids (C101/100, TAAB Laboratories Equipment Ltd., Berks, England).



**Figure 2.3:** An ultramicrotome with a diamond knife and a water tray was used for the thin sectioning of the samples (thickness from 70 nm and up). The thin sections were collected from the water surface onto 200-mesh copper grids with a carbon support film. Photos: Dick Gillberg, courtesy of SP Food and Bioscience.

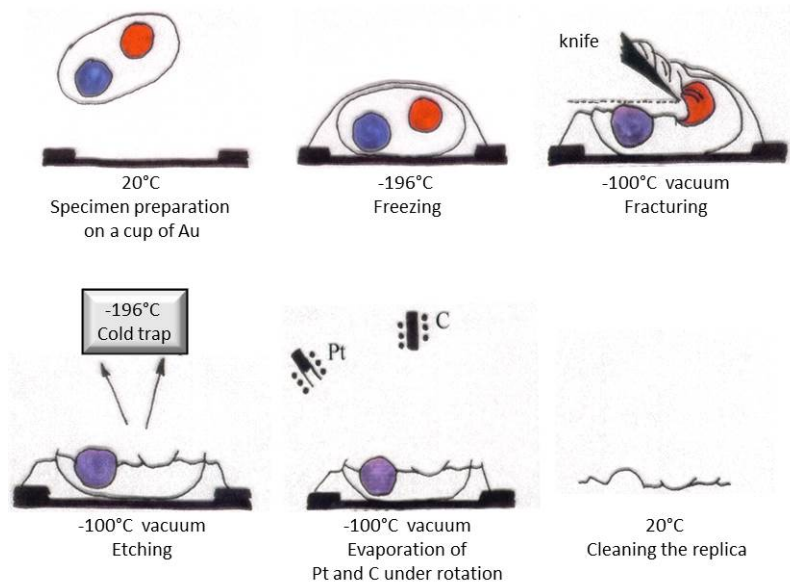


**Figure 2.4:** Schematic image of the procedures of freeze fracture and freeze etching. Image courtesy of Annika Altskär, SP Food and Bioscience.

## 2.4 Freeze fracture and freeze etching

It is crucial to ensure that the sample preparation does not affect the structure of the material. The effect of sample preparation can be evaluated by comparing the result of more than one sample preparation technique and also by other known characteristics of the material.

As a complement to the plastic embedding, the freeze-fracture and freeze-etching methods[46] were used for comparison. In short (see figure 2.4), the sample is plunge frozen in liquid propane ( $-196\text{ }^\circ\text{C}$ ), fractured at a temperature of  $-100\text{ }^\circ\text{C}$ , etched for two minutes and shadowed with platinum and carbon, respectively. The obtained replica is then removed from the original sample.

## 2.5 TEM and STEM contrast mechanisms and equipment

In traditional visible light microscopes, photons in the form of visible light are used for creating images of microscopic objects. The resolution of an image is often defined as the minimum distance between two points that are still perceived as two points instead of one. A common estimation of the possible resolution ( $\delta$ ) in a microscope is the Rayleigh criterion,

$$\delta \approx \frac{1.22\lambda}{\beta}, \quad (2.1)$$

where  $\lambda$  denotes the wavelength of the photons, and the  $\beta$  denotes the semi collection-angle of the magnifying lens. This criterion sets the maximum possible resolution for a visible light microscope to approximately 300 nm[47]. One way to push the resolution even further is by using electrons with shorter wavelengths instead of photons. Electron microscopy is one of few techniques that can provide both spatial resolution on the sub Ångström scale and chemical information with high spatial resolution, i.e. on the sub nanometre scale.

Transmission electron microscopes were used for acquiring bright field TEM and high angle annular dark-field (HAADF) STEM (HAADF-STEM) micrographs of the sectioned samples. An image is formed by magnetic lenses, and can be displayed on a fluorescent screen or with a charge-coupled device (CCD) camera, after the electron beam have interacted with the specimen, as shown in figure 2.5. Different other types of detectors (e.g. the HAADF detector) could also be used when creating an image.

The dominating contrast mechanism for amorphous materials (as both the silica gel and the embedding material is) is the mass thickness contrast. It originates from the difference in the degree of electron scattering by heavier and lighter elements. Heavier elements will scatter a higher proportion of electrons to higher angles compared to lighter elements. An objective aperture can be used to select different

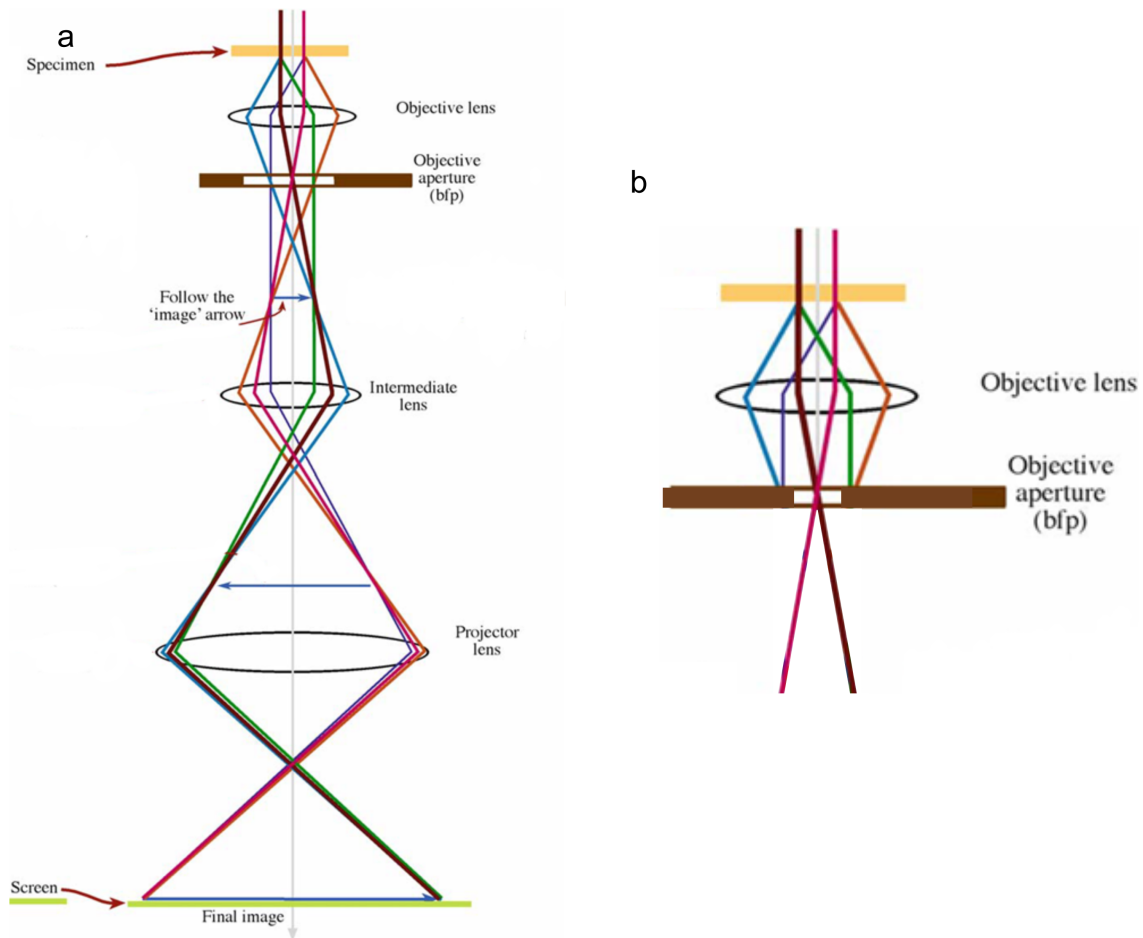


**Figure 2.5:** (a) A schematic image of the beam paths and main parts of a TEM. (b) The objective aperture size and position can be varied in order to block beams scattered to a high angle by the specimen, increasing the contrast in the acquired images. Image modified from Williams and Carter[47].

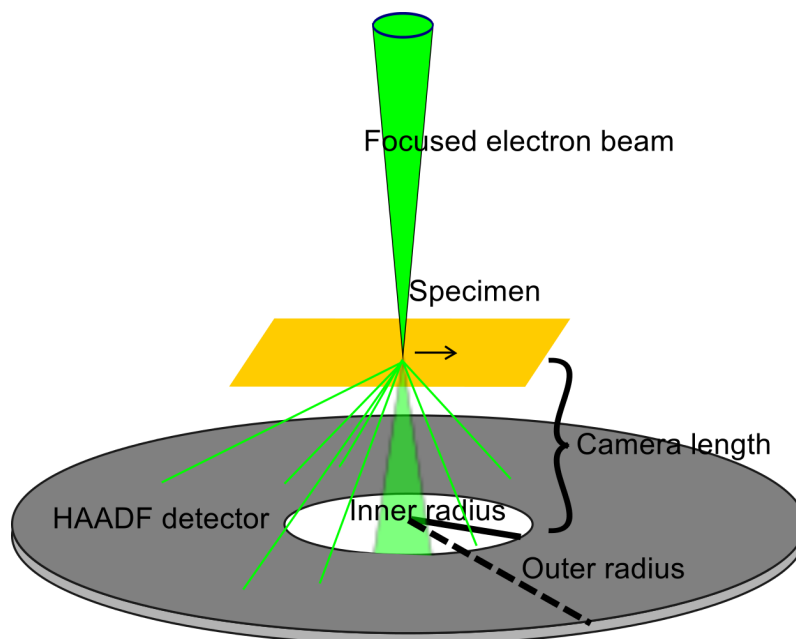


**Figure 2.6:** A schematic image of the principle of HAADF-STEM imaging. A focused electron beam is scanned over a part of the specimen. The thin green lines represent scattered electrons. Electrons scattered to high angles by the sample will be detected by the HAADF detector. The number of detected electrons for a specific position of the beam will determine the intensity value for the corresponding pixel in the acquired image. The camera length is the virtual distance between the specimen and the detector.

portions of the scattered electrons, enhancing the contrast of the image (see figure 2.5b). For STEM imaging, an annular HAADF detector is placed in one of the focal planes collecting electrons scattered at higher angles, while the direct beam or less scattered electrons will not be recorded, see figure 2.6. For the silica gel specimens (which have an even thickness), the silica particles will appear darker compared to the embedding plastic in TEM mode, and lighter than the embedding plastic in HAADF-STEM mode[47].

A TEM and STEM specimen needs to be thin in order for the beam to be able to penetrate the whole thickness of it. The image will be a 2D projection of the 3D structure present within the specimen. A typical specimen thickness in this work was between 70 and 300 nm.

The different TEMs used for imaging the ultramicrotomed sections were a Titan 80-300 field emission gun (FEG) (FEI Company, Eindhoven, Netherlands) operated at an acceleration voltage of 80 kV or 300 kV, a Tecnai G2 LaB<sub>6</sub> (FEI Company, Eindhoven, Netherlands) operated at an acceleration voltage of 200 kV, and a Leo 906E with a tungsten filament (LEO Electron Microscopy Ltd., Oberkochen, Germany) operated at an acceleration voltage of 80 kV.

### 2.5.1 TEM Tomography

A TEM produces a 2D projected image of a specimen. This means that a prominent 3D structure in the specimen could result in micrographs that are difficult to interpret. The fact that the human brain is an expert of making assumptions based on data collected by our eyes, further complicates things. A way to visualise the full 3D volume of a specimen is to use tomography in an electron microscope. Electron microscope tomography was first used within the biological sciences, and was awarded two Nobel Prizes, one in 1972 and one in 1982[48]. During the 1990's, great progress was made in the area of automating the image acquiring process[49]. The starting point for usage within the physical sciences came in the the early 21st century, as it was implemented and described by Midgley et al. in 2001[50], and Midgley and Weyland in 2003[51]. The technique is continuously developed, for example by using known information about the sample.

The techniques of 3D TEM and 3D STEM are both powerful for determining the 3D structure on the nanometer scale. Although the principle of tomography itself is fairly straight forward, retrieving high resolution tomograms is demanding since it requires careful sample preparation, imaging of a possibly beam sensitive sample with low contrast, image alignment using cross correlation, reconstruction and visualisation. In this work, 3D STEM was used to image colloidal silica nanoparticle gel samples with different pore sizes.

In electron tomography, an image series of the specimen is collected either by imaging the same specimen when tilting the holder, or by using images of identical objects rotated in a variety of directions[52]. This approach is applicable when imaging several identical biological specimens, but not when working with irregular porous structures. For unique samples, a tilting approach is necessary. Tilting can be performed in different ways, and in this work a single axis tilting method was used. In single axis tilting, the specimen is tilted between two maximum tilt points, e.g. from  $+70^\circ$  to  $-70^\circ$ [48]. The tilting can have either the same increment angle between each exposure (linear) or a smaller increment angles at high tilt angles and larger increment angles at low tilt angles (Saxton scheme)[53]. The Saxton scheme was chosen in order not to oversample data from the lower tilt angles and not to undersample data from the higher tilt angles. For the collection of the tilt series, the Advanced Tomography Holder Model 2020 (E.A. Fischione Instruments, Inc., Export, PA, USA), a specially adapted single tilt holder, was used, enabling a tilt range between  $+80^\circ$  to  $-80^\circ$ .

After the data collection, any distorted images need to be removed and the remaining images need to be aligned. The alignment is done by a cross correlation procedure of the images, where low-pass and high-pass filters are used for alignment perfection. After the fine tuning of the alignment, the 3D structure of the imaged specimen can be reconstructed using the Radon transform[54].

The software Xplore3D and Inspect3D (FEI Company, Eindhoven, Netherlands), and occasionally IMOD[55] were used for image acquisition, cross-correlation align-

ment and reconstruction of a 3D volume from within the specimen. The resulting reconstructions were visualised and if necessary, filtered and thresholded, using Amira 5.3.2 and Avizo 9 (both from Visualization Sciences Group, an FEI Company).

### Mathematical principles of reconstruction from STEM images

The mathematical solution for finding the 3D reconstruction from projections was found as early as 1917 by Radon[54]. However, the computational power needed for performing the necessary calculations for structural reconstruction has only been around for approximately 40 years[48].

In order for an imaging technique to be suitable for tomographic reconstruction, the projection requirement must be fulfilled, meaning in principle that the tilted projections need to have a monotonic intensity relationship[56]. An example of a technique that fulfils this requirement of monotony is the STEM imaging, where more material in the direction of the beam will correspond to a higher detected intensity value in the image.

In order to reconstruct the imaged object, the Radon transform is used. The details of the Radon transform are presented in the 1917 article by Radon[54]. The general principle of the Radon transform, however, is usually explained as going from one to two dimensions, which is equivalent to going from 2D to 3D. The Radon transform ( $R$ ) is then a mapping of a function  $f(x, y)$ , which describes a real space object ( $D$ ) by the projection, or line integral, through  $f$  along all possible lines  $L$  with unit length  $ds$ ,

$$R = \int_L f(x, y) ds, \quad (2.2)$$

see figure 2.7 for clarification. In practice, the set of all 2D images collected during a tilt series in the STEM can be seen as a discrete sampling of the Radon transform. Hence, using the inverse Radon transform on the projections will result in a reconstruction of the imaged object if the sampling frequency is high enough[51]. The inverse Radon transform is the foundation of the different direct algorithms available for tomographic reconstruction.

There are several different reconstruction algorithms[48]. Two of the most common ones are the weighted back-projection (WBP) and the simultaneous iterative reconstruction technique (SIRT) algorithms. In this work, the SIRT algorithm was used since it is more accurate than the WBP method. The SIRT algorithm changes the densities of the reconstructed object by using all the projected images simultaneously. As the next step, the mean density value of the original object is compared to the mean density of the volume under reconstruction, and the reconstruction values are scaled in order for its mean density to coincide with the mean density of the original. These steps are repeated iteratively[57]. SIRT is one of the reconstruction algorithms embedded in the Inspect3D software, and is generally used in this work.

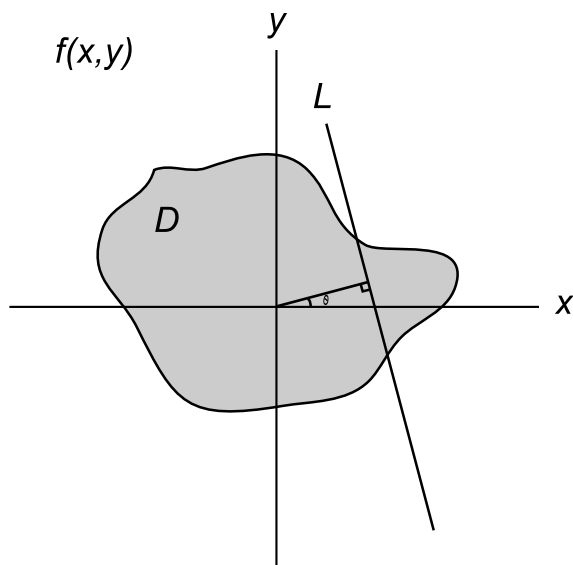


**Figure 2.7:** An illustration of the principle of the Radon transform (from 1D to 2D).  $D$  is the object to be reconstructed, displayed in a cartesian coordinate system representing real space. The line  $L$  shows just one representation of a line integral (equivalent to a projection), through the object  $D$ . The Radon transform can be visualised as the integration through  $D$  along *all* possible line integrals,  $L$ , at a specific angle  $\theta$  to the  $x$ -axis.

In recent years, several algorithms where prior knowledge of the samples is used during the reconstruction process, have been presented. Examples of this are the compressed sensing algorithm (which applies to samples that can be sparsely represented)[58], the discrete tomography algorithm (where the number of gray levels reconstruction has to be properly estimated)[59] and the PORES algorithm (where the fact that the material is porous is known)[60]. A useful feature of all these algorithms is that the acquiring procedure of the tilt series does not have to be altered in any way in order to use them. One or several of these new algorithms could prove useful for this work in the near future.

### Beam sensitivity and possible artifacts

All materials are more or less sensitive to the electron beam[61]. Due to the risk for beam damage, the total exposure time and voltage during a tilt series acquisition should be kept to a minimum, while still maintaining the amount of data required for sufficient quality of the reconstruction of the sample.

When imaging plastic embedded materials, it is especially important to have this in mind, since the most common form of beam damage is shrinking of the specimen in one or several of the spatial directions[61]. In the 3D case, this shrinkage can be seen as "y"-shaped features in the reconstructed sections, see figure 2.8. It affects



**Figure 2.8:** An example of how shrinking during tilt series acquisition may manifest itself in the reconstruction. The reconstructed particles are shaped like the letter Y. Screenshot from the Tilt Axis Adjustment step in Inspect3D, from a tilt series of Gel 1.

the resolution of the tomogram. Another difficulty for plastic embedded materials is the risk of contamination. Especially in STEM mode, when the beam is repeatedly focused at one position between scans, there could be a build-up of hydrocarbons, distorting the contrast of the specimen locally or on a larger area.

When imaging the single silica nanoparticles, a higher voltage could contribute to altering the particle shape. Hence, when imaging the single particles of Gel 2 and 3, a lower voltage of the electron microscope was used (80 kV on the Titan).

In tomography, effects in the reconstruction appearing as a consequence of the data acquisition rather than the sample itself are denoted artefacts. The most common artefact in electron tomography originates from the missing wedge (MW), see figure 2.9 and 2.10. It originates from the specimen holder restraining the possible tilt range, meaning that information from the highest tilt angles is lost. High-tilt information can also be lost due to a decrease in image quality for higher tilt angles, see figure 2.9. The MW artefact results in the reconstructed tomogram having an elongation in the thickness direction, i.e. parallel to the electron beam at  $0^\circ$  tilt.

Another factor having a large impact on the resolution and accuracy of the reconstructed structure is the alignment of the images in the tilt series. The tilt axis needs to be in the centre of each image, and the ever-present small horizontal holder movements needs to be counteracted by image alignment. The images were aligned by a cross-correlation procedure in Inspect3D. Poor alignment will inevitably result in a poor structure reconstruction.

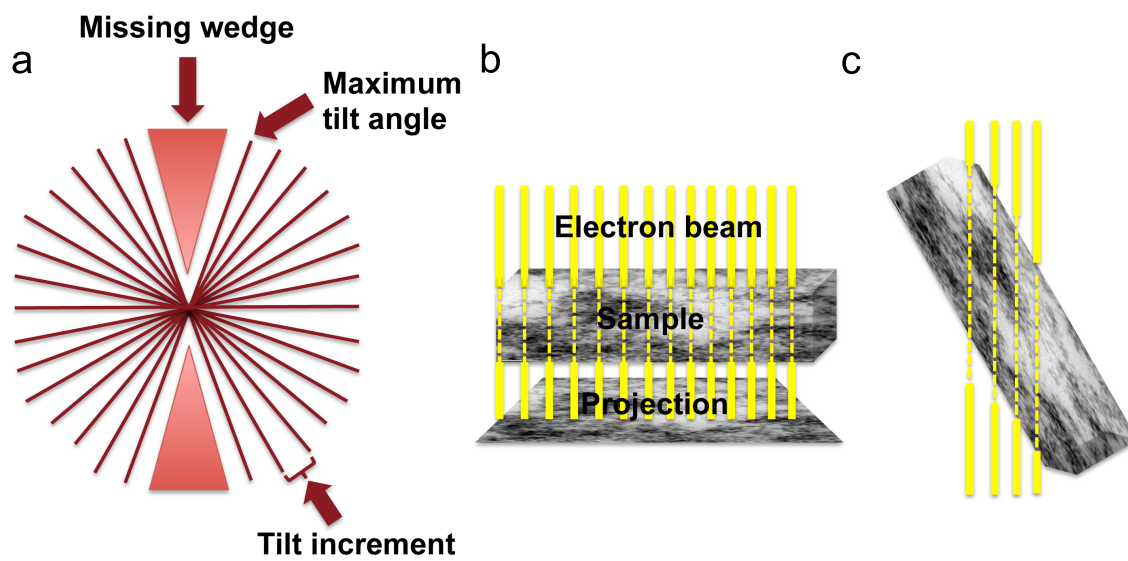


**Figure 2.9:** (a) During the tilting process, the specimen holder usually limits the tilt range. Information from the highest tilt angles will therefore be lost. This MW artefact manifests itself as the reconstructed tomogram having an elongation of features in the direction parallel to the electron beam at  $0^\circ$  tilt. (b-c) When the sample slice is tilted with respect to the electron beam, the distance travelled by the electrons within the material will be larger and the electrons will scatter more, resulting in a poorer image quality. This effect adds to the missing wedge effect, since images of too poor quality cannot be used for the reconstruction of the structure.

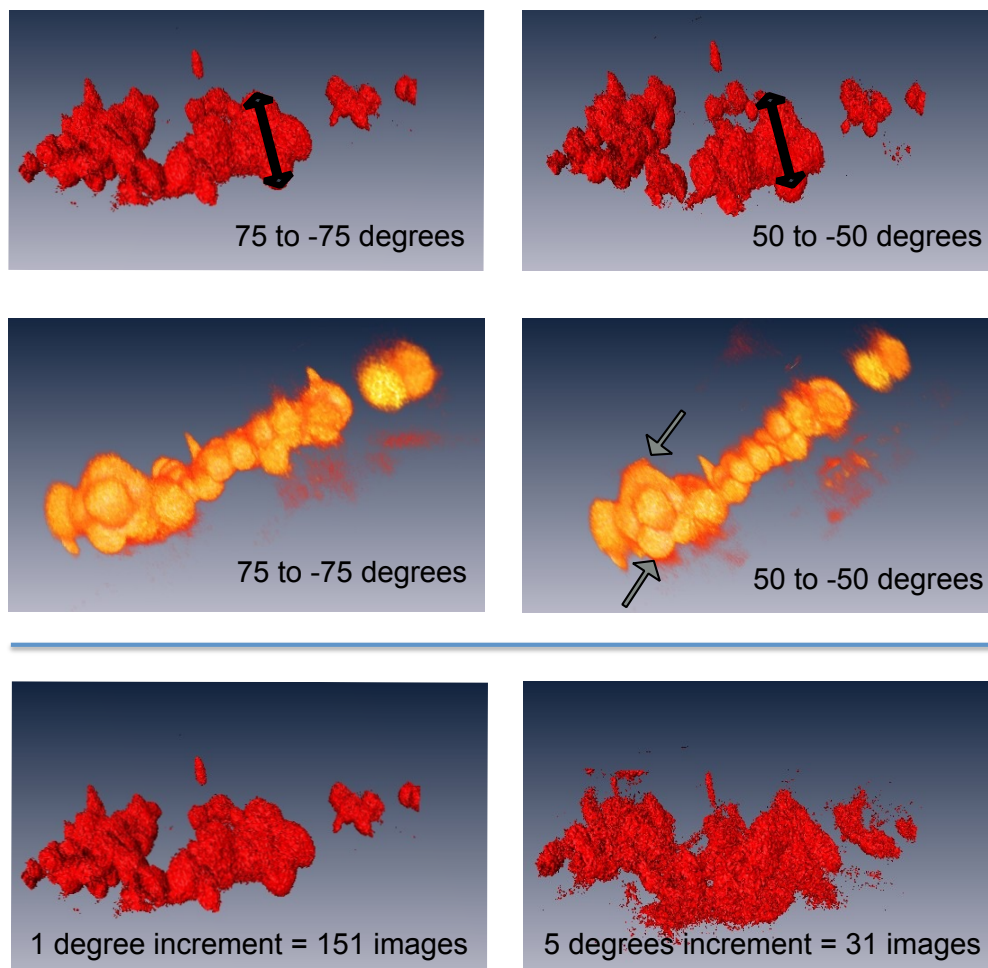


**Figure 2.10:** Examples of the elongation and flaring effects due to the MW artefact, and the image quality loss due to large increment between tilts. All images show high magnification constructions of a 70 nm slice of Gel 1 (particles approximately 20 nm in diameter), from 3D STEM on Titan at an operating voltage of 300 kV. The acquisition tilt range was from  $+75^\circ$  to  $-75^\circ$  with a linear tilt increment of  $1^\circ$ . **Upper row:** Comparing the right and the left images, elongated structures in the missing wedge direction can be seen. The arrows have the same length. The particles are visualised by their isosurfaces. **Center row:** Comparing the right and the left images, flaring in the missing wedge direction can be seen. The arrows point to the most prominent flares. The particles are visualised by volume rendering. **Lower row:** Comparing the right and left images, poor particle definition due to too larger increment steps during acquisition can be seen. The particles are visualised by their isosurfaces.

## 2.6 Statistical analysis models

### 2.6.1 Stereological image analysis

Stereology is a mathematical and statistical method for determining 3D characteristics from 2D data. The strength of this method is the use of a mathematically defined description of a pore, regardless of its morphology.

This data can ideally be an infinitesimally thin section from a 3D structure. The development of the techniques started in the 1960's, but the mathematical mindset of geometrical probability goes back several hundred years. Due to the relative ease in acquiring large quantities of 2D images, compared to 3D ones, the stereology approach is often used for finding microstructural information in e.g. food science[62] and medicine[63]. These methods are also widely used in the area of pathology[64],[65] and have also successfully been used for the characterisation of e.g. kinetically trapped phase separated biopolymer mixtures[66].

Stereology provides theoretically unbiased statistical methods for estimating the volume of arbitrarily shaped structures (based on 2D images)[67]. In this work, it was chosen for estimating the pore size of the different silica gel samples.

The volume-weighted mean volume (VWMV) is an unbiased estimator, where no assumptions of particle or pore shape have to be made[68]. The only requirement is that the sections are recorded from randomly chosen regions, and that the material is geometrically isotropic. Using this estimator, we also define the concept of a pore. Since the method is volume weighted, it is well suited for use within mass transport studies.

The definition of the stereological estimator: VWMV, also called "star volume", is stated in Gundersen et al.[64] as "the mean volume of all parts of an object that can be seen unobscured in all directions from a particular point". Hence, the VWMV is condensed to one single mean value for the structure. The VWMV is calculated as

$$V^* = \frac{\pi}{3} \bar{l}_0^3. \quad (2.3)$$

Here,  $V^*$  denotes the VWMV and  $l_0$  denotes the intercept length, i.e. the length of an intercept randomly passing through a void within the sample, see figure 2.11.

Using this method, it was assumed that the materials were geometrically isotropic and that the imaging sites on the gel sample were selected with equal probability of being sampled. The systematic, random selection is a prerequisite for using stereological analysis methods for unbiased volume estimation of arbitrarily shaped structures[67].

The interfacial area ( $S_V$ ) of the silica surface of the pores were also estimated using stereology. This area can be determined as

$$S_V = 2 \frac{P}{l_0}, \quad (2.4)$$

where  $P/l_0$  denotes the numbers of intersection points per intercept length[62].

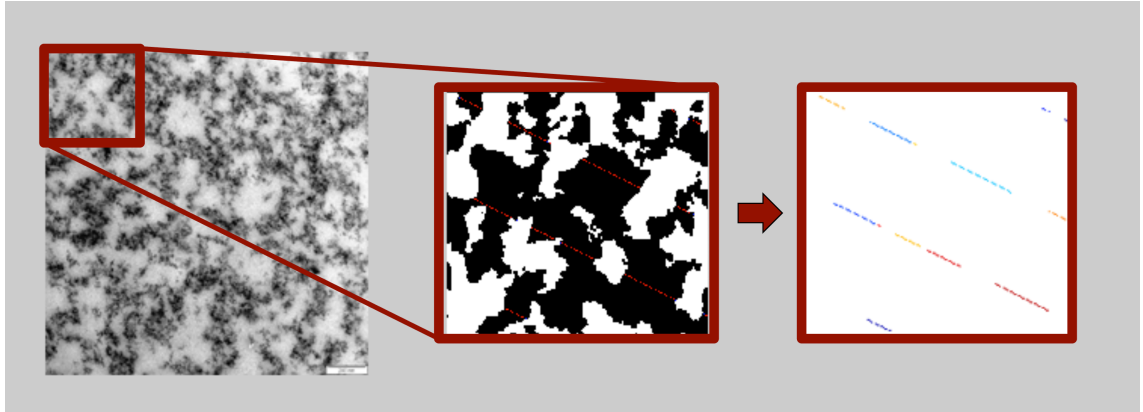


**Figure 2.11:** Illustration of key concepts in star volume estimation of pore volume. The projected (S)TEM image is binarised and intercepts (superimposed red lines) are introduced with 200 pixels spacing. The isolated intercepts are shown in colour for clarity.

2D images on approximately 70 nm thick sections of the embedded silica nanoparticle gels were used. Because of the specimen thickness, the VWMV will be to some extent underestimated. For the quantitative analysis, the TEM or STEM images (grayscale) were converted to binary (black or white) images, by a series of filter steps performed in MATLAB (The MathWorks, Inc., Natick, MA, USA).

### 2.6.2 The maximum log-likelihood method for 3D simulations from 2D images

A statistical approach based on the log-likelihood of the response observed at each pixel was used when investigating the intensity in 2D projections as a function of mass thickness (i.e. the fraction of silica in the direction of the electron beam, for each pixel in the image). The intensity function can be estimated as e.g. linear or as a power law. The power law is chosen to illustrate the estimated function here.

When estimating the intensity ( $I$ ) as a function of silica mass thickness ( $\alpha$ ), there are several unknown parameters that need to be estimated: the background intensity of the image ( $b$ ), the power constant of the function ( $\beta$ ), and a constant  $c$ . The equation can then be presented as

$$I(\alpha) = b + c\alpha^\beta, \quad (2.5)$$

and is specific for each pixel. Since  $\alpha$  denotes the mass thickness of the investigated simulated micrograph, it also includes the underlying information of the particle positions and the number of particles, although it is not explicitly written in the equation.

The next estimation step is the particle centre positions, which are denoted  $[\mathbf{x}_0, \mathbf{x}_1, \dots, \mathbf{x}_N]$ , and the number of particles ( $N$ ). A normally distributed noise term is

finally added as a factor in the intensity function (equation 2.5), and the variance ( $\sigma$ ), of this noise term also needs to be estimated.

In general, when estimating the expectation of normally distributed observations using a log-likelihood approach, the estimation can be obtained by determining the maximum of the log-likelihood function, which is the same as the arithmetic mean of the observations. However, there is not always an analytical solution available, especially when a large number of parameters is involved. This is the case for the intensity estimation used here, where the log-likelihood function ( $l$ ) summed over all pixels ( $n$ ), is given by

$$l(N, \beta, \sigma, b, c, \mathbf{x}_0, \mathbf{x}_1, \dots, \mathbf{x}_N) = -n \log(\sqrt{2\pi}\sigma) - \sum_{i=1}^n \left( \frac{1}{2\sigma^2} (I_{0i} - I_i)^2 \right) \quad (2.6)$$

which requires a numerical maximization [69]. Here,  $I_{0i}$  denotes the intensity value for that particular pixel in the original micrograph, and  $n = |M|$  in **Paper II**.

In this approach, circular discs representing the particles were positioned within an image frame before maximizing the log-likelihood function to estimate the mentioned variables. After this step, the log-likelihood function was maximized again, after changing the positions of the discs. Iteration between these two steps was performed until a maximum was reached.

## 2.7 Mass transport measurements

### 2.7.1 Pressure driven flow speed measurements

Open-ended test tubes were used to measure the steady state flow speed of the silica gel as previously described [26, 70]. The flow is here defined as flow rate of liquid per unit area, given in  $\text{m}^3\text{m}^{-2}\text{s}^{-1}$ , or  $\text{ms}^{-1}$ .

In short, the gel samples were gelled in open-ended borosilicate glass tubes with an 8 mm inner diameter. The gel was resting on a polyester mesh in order not to escape from the glass tube. The total height of the gel sample within the glass tube was 30 mm, and the meshed end was in contact with the bottom of a Petri dish filled with 0.9 M NaCl solution of 8 mm depth. The column was filled with 50 mm of 0.9 M NaCl aqueous solution on top of the gel. The flow rate through the gel was measured by marking the position of the liquid surface, one to two times a day. A parafilm seal, slightly perforated to eliminate underpressure, made evaporation from the top of the column insignificant. Petri dishes were replenished by MilliQ water every day to compensate for water evaporation and all experiments were carried out at room temperature.

### 2.7.2 Nuclear magnetic resonance imaging diffusometry

A method that provides a non-invasive, convenient, multi-component substance selective method for measuring translational motion is nuclear magnetic resonance (NMR) diffusometry. It provides information about the global diffusion properties in basically any type of liquid-like material. Diffusion coefficients down  $10^{-17}$   $\text{m}^2/\text{s}$  may be observed with good accuracy during optimal conditions. The Larmor frequency is dependent on the magnetic field. In NMR diffusometry, a magnetic field gradient is applied. Thus, the Larmor frequency reports about the spatial position of the molecules. During diffusion, the molecule passes areas with different magnetic fields due to the gradient. The phase shift of the Larmor frequency can be correlated to the diffusion rate[71]. NMR diffusometry can also give information on the microstructure in which molecules are diffusing as well as other events, i.e. on-off rates of adsorption and desorption, aggregation states, hydrodynamic radii, molecular weight distribution, fraction of surface bound versus freely diffusing molecules.

The self-diffusion coefficients of the gels were measured one to two weeks after gelation, using a Bruker Avance 600 spectrometer (Bruker, Karlsruhe, Germany) and a Diff30 diffusion probe with a maximum gradient strength of 1200 G/cm.



## Chapter 3

# Results and discussion

In this chapter, the main results are described and discussed. The results are based on data presented in the included papers, and some unpublished data from work in progress concerning the 3D imaging of the silica nanoparticle gels.

### 3.1 Ensuring an appropriate sample preparation method

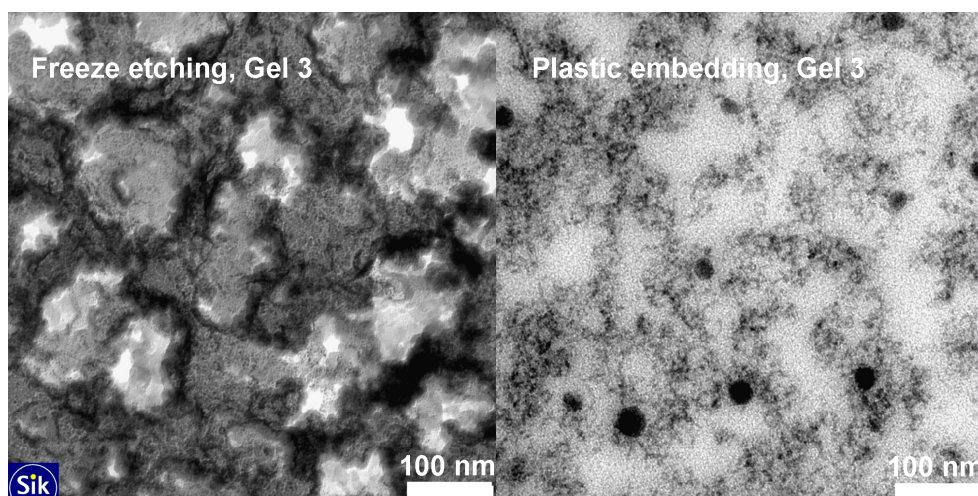


**Figure 3.1:** A comparison between the freeze etching and the plastic embedding methods, illustrating both the similarities in structure detected using the two methods, and the challenge of a quantitative comparison of the two techniques. In the freeze etched sample, the light grey and white areas correspond to the light areas in the plastic embedded sample. The darker, more evenly grey structures in the freeze etched sample, visualises the aggregated silica structure, which can be seen as the darker structure in the plastic embedded sample. When taking the differences in the two preparation techniques into account, no apparent differences in material structure can be detected between the two preparation techniques.

Figure 3.1 shows a plastic embedded Ge 3 specimen and freeze fractured replica of the corresponding sample. As seen in figure 3.1, the different preparation techniques present very different types of information. For example, the replicas that are investigated in the microscope represent the surface topography of a freeze fractured and freeze etched gel sample. This is in contrast to the embedded and microtomed samples, where the images are projections of thin sections. In the projected TEM images, an apparent pore structure is easily seen but it is important to remember that this structure will be affected by the section thickness.

A comparison between results from freeze fracture with freeze etching preparation and from plastic embedding of the gels showed that the volume fraction of silica nanoparticles, and the connectivity of the structure seems to be independent of preparation technique.

### 3.2 Sample selection based on porous length scale

Three gels were selected based upon the length scale of their porous network structure, in order to reflect a range of length scales spanning from a diffusion dominated region to a region dominated by viscous flow. The gels were chosen for detailed characterisation of their porous nanostructure, and their flow and diffusion properties. The structural characterisation was performed in both 2D and 3D .

**Table 3.1:** Pore size estimation chart. The three selected gels are marked in italics, and have a silica percentage of 9.0 wt%. The sphere diameter data is from Abrahamsson et al.[26]<sup>a</sup> and AkzoNobel, PPC AB<sup>b</sup>.

Product name	Est. pore size [nm]	Particle diameter [nm]	SiO <sub>x</sub>	pH	[NaCl]
Bindzil 40/130	500 nm	22±5.0 <sup>a</sup>	9.0 wt%	7.8	0.9 M
<i>Bindzil 40/130</i>	<i>430 nm</i>	<i>22±5.0<sup>a</sup></i>	<i>9.0 wt%</i>	<i>7.8</i>	<i>0.5 M</i>
Bindzil 40/130	430 nm	22±5.0 <sup>a</sup>	9.0 wt%	4.0	0.9 M
Bindzil 40/130	430 nm	22±5.0 <sup>a</sup>	9.0 wt%	4.0	0.5 M
Bindzil 40/130	370 nm	22±5.0 <sup>a</sup>	5.0 wt%	7.8	0.9 M
Bindzil 40/130	240 nm	22±5.0 <sup>a</sup>	5.0 wt%	7.8	0.5 M
Bindzil 30/360	150 nm	7 <sup>b</sup>	9.0 wt%	7.0	0.9 M
GB3000	145 nm	3.6 <sup>b</sup>	6.0 wt%	7.0	0.9 M
<i>Bindzil XP1</i>	<i>130 nm</i>	<i>5.0<sup>b</sup></i>	<i>9.0 wt%</i>	<i>7.0</i>	<i>0.9 M</i>
<i>GB3000</i>	<i>60 nm</i>	<i>3.6<sup>b</sup></i>	<i>9.0 wt%</i>	<i>7.0</i>	<i>0.9 M</i>

The selection of these gels was based on an initial screening of the approximate pore sizes of the gels. The pore size estimation was performed using TEM images of the embedded gels, and manually positioning four to five circles into the images in a way that the circles were drawn as large as possible without overlapping any areas of silica structure. This procedure was repeated for a few images of each sample and

### 3.3 Pore size effects on flow and diffusion through nanoporous silica gels 27

the pore size estimation was then defined to be the median diameter of the circles for each sample. The data for all samples are presented in table 3.1.

Since diffusive mass transport can be considered a function of the volume accessible to the solute[72], the silica solid volume fraction of the gels was also considered when selecting the samples.

### 3.3 Pore size effects on flow and diffusion through nanoporous silica gels

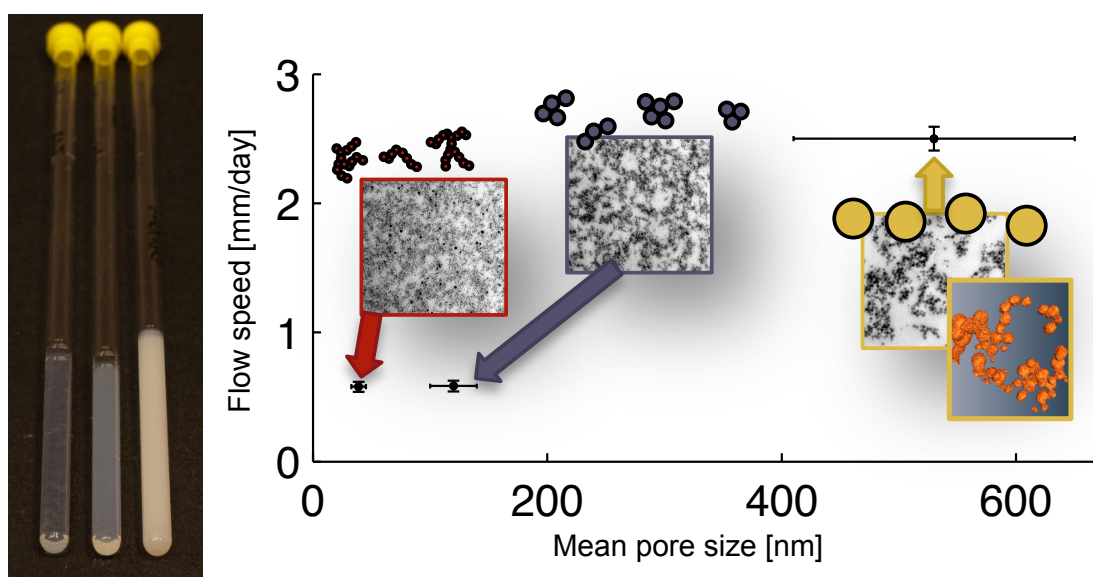


**Figure 3.2:** The influence of pore size distributions on flow speed was studied in three colloidal silica gels of equal volume fraction but with different primary particle size and morphology.

We have investigated water transport in the transition region between flow and diffusion in silica gels (figure 3.2). Three silica nanoparticle gels with large, medium and small pores, respectively, were chosen purely based on the pore size expected from bright field TEM (BF TEM) micrographs, as described in section 3.2. All gels had a volume fraction of 4.1 vol% (equivalent to 9.0 wt%) silica but different primary particle size and morphology. This diversity in particle morphology resulted in large pore structure diversity. The gels were characterised with respect to the morphology of the primary particle size and shape, as well as the mean VWMV and the PSD of the gel structures.

For three different nanoporous silica gels, we investigated the particle size and morphology, as well as the direct connection between pore size and mass transport. The primary particles and the pore structure was imaged using TEM and STEM.

It can be clearly seen that all the samples are built up from silica spheres, but that the pre-aggregated particles are distinctly different concerning aggregation and neck-formation status, compared to the not pre-aggregated particles of Gel 1, see figures 3.3-3.5.

For interfacial area, pore size and PSD analysis, two approaches were used: The stereological methods (VWMV and intrinsic area), and a straightforward geometrical approach, where circles of a decreasing radii were systematically fitted where they encountered no particles. Since the geometrical method and the stereological method for pore size analysis are intrinsically different, they are not directly comparable to each other. A practical advantage of using the VWMV method is that it is volume-weighted, meaning that the larger pores will have a larger impact on the mean pore size value. Since mass transport by flow is highly dependant on the size of the pores, the volume-weighting proved meaningful. However, the VWMV technique will not provide any size distribution of the pores. The benefit of using the geometrical approach on the other hand, is that it provides distribution data on all of the fitted circles (not only a mean value for the whole gel). The values of the methods differ by approximately a factor of two. Both methods will in practice underestimate the pore sizes due to the micrographs being projections of a thin section.

No indications of anisotropy was found in the microscopy data of any of the silica gel samples. Anisotropy could have manifested itself as repeatedly occurring directionally dependancy of the microscopic structure. Images were analysed both before and after a 90° rotation, with no significant difference in VWMV. This further confirmed the assumption of isotropy in the samples, and the VWMV estimator could be used.

The diffusion coefficients of the gels were determined using NMR diffusometry and gravitationally driven steady state flow was determined using the previously described setup[26], where the gravitational pull forced water to penetrate the columns of the specific gels. The salt concentration of the gels was adjusted to the same level for all samples, in order for the ionic strength not to interfere with the permeability tests.

We concluded that two of the three samples contained particles that often formed multiplets of several pre-agglomerated spheres, or particles that were almost exclusively present as branched and stranded agglomerates of several silica spheres, see figures 3.4 and 3.5.

All samples presented very different pore sizes and PSDs (see table 3.2 and figure 3.6), which would predict the mass transport to differ accordingly. However, two of the three samples had near identical convective flow data. This contradiction is something that needs to be investigated further in order to fully understand how the nanostructure of a porous material affects the mass transport. From this, we conclude that for gels having a VWMV less than approximately 120 nm, the water transport will be independent of pore size.

The explanation for the above mentioned conclusion could also be found in the 3D structure of these gels. Particularly the connectivity of the pores, both through

### 3.3 Pore size effects on flow and diffusion through nanoporous silica gel<sup>29</sup>

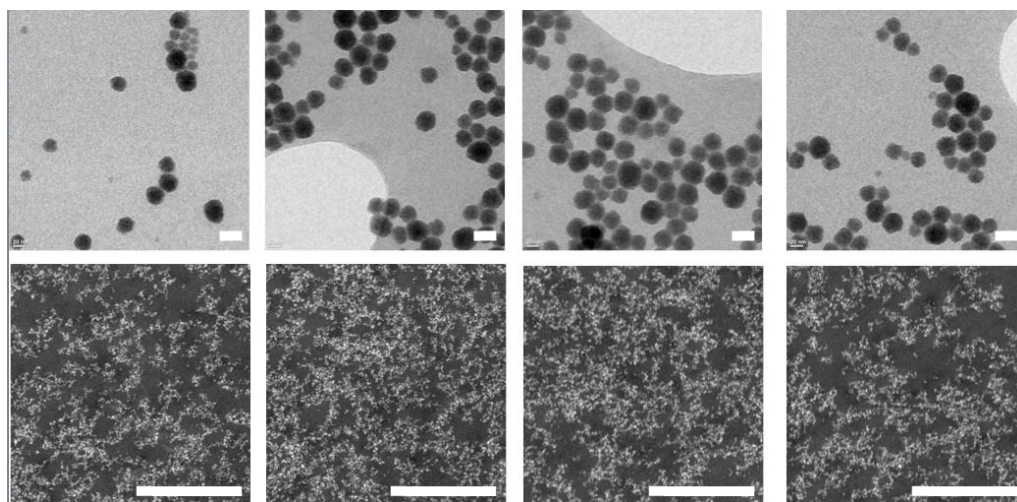


**Figure 3.3:** TEM images of the primary particles, Bindzil 40/130, in the upper row. The particles appear dark and the holey carbon film in the background appear brighter. Bindzil 40/130 consists of spherical particles (scale bars are 40 nm). In the lower row, the gel structure of Gel 1 can be seen in STEM micrographs (scale bars are 1  $\mu\text{m}$ ). Here, the particles appear bright and the background appears dark.

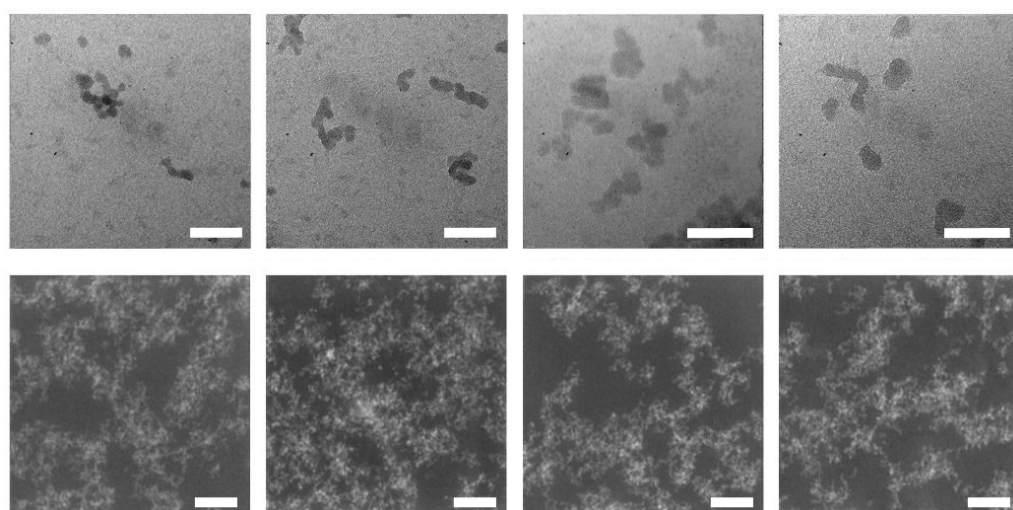


**Figure 3.4:** TEM images of the primary particles, Bindzil XP1, in the upper row. The particles appear dark and the holey carbon film in the background appear brighter. Bindzil XP1 consists of particle multiplets (scale bars are 40 nm). In the lower row, the gel structure of Gel 2 can be seen in STEM micrographs (scale bars are 100 nm). Here, the particles appear bright and the background appears dark.

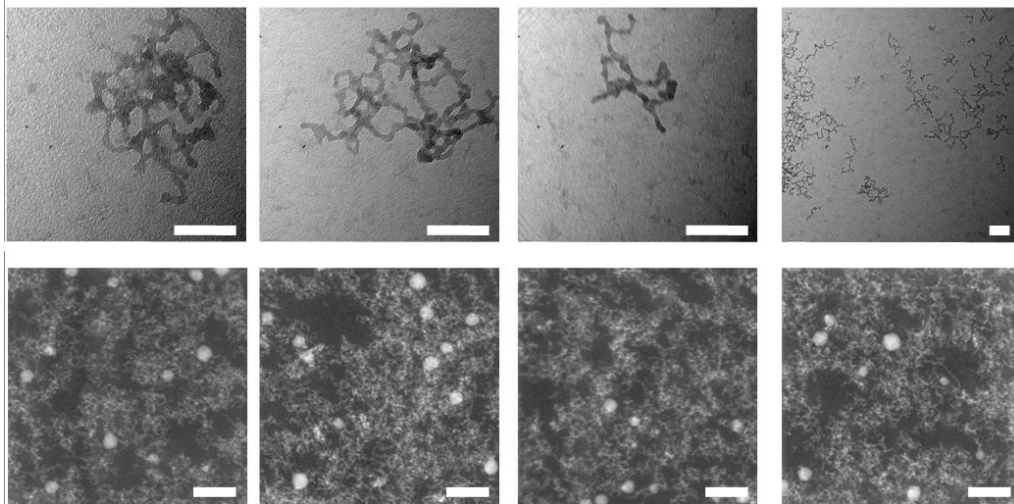


**Figure 3.5:** TEM images of the primary particles, GB3000, in the upper row. The particles appear dark and the holey carbon film in the background appear brighter (scale bars are 50 nm). GB3000 particles are branched and have a complex structure. In the lower row, the gel structure of Gel 3 can be seen in STEM micrographs (scale bars are 100 nm). Here, the particles appear bright and the background appears dark.

**Table 3.2:** Structural gel parameters for the three samples. The VWMV and the arithmetic mean diameter (AMD) for fitted circles, were used as pore size indicators. The VWMV is presented as the diameter of an equivalent sphere, and the standard error amongst the micrographs is shown. For the AMD, the standard deviation amongst all individual pores is shown. The intrinsic surface areas (ISA) of the samples are also shown, together with the standard error.

Sample	VWMV [nm]	AMD [nm]	ISA [ $\mu\text{m}^{-1}$ ]
Gel 1	530 $\pm$ 120	310 $\pm$ 180	13 $\pm$ 1.7
Gel 2	120 $\pm$ 20	58 $\pm$ 32	40 $\pm$ 4.1
Gel 3	39 $\pm$ 6.3	18 $\pm$ 15	150 $\pm$ 7.9

### 3.3 Pore size effects on flow and diffusion through nanoporous silica gels

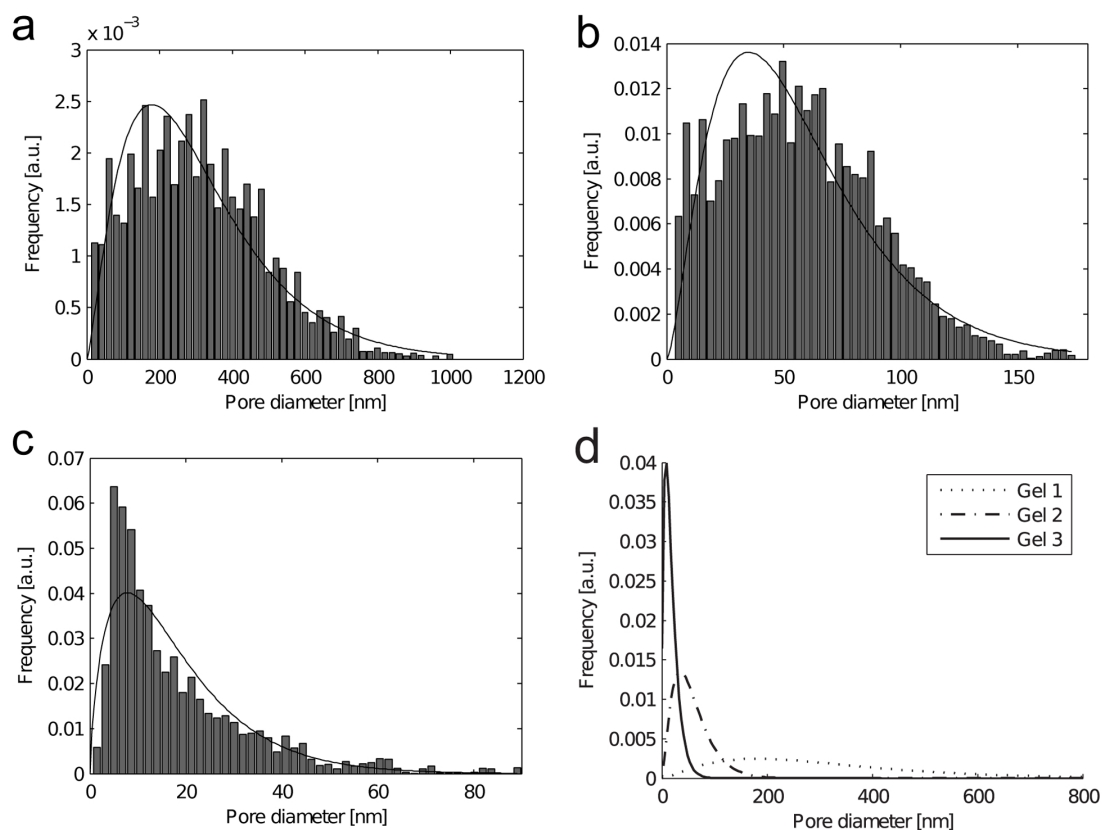


**Figure 3.6:** (a-c) Pore diameter distribution of Gel 1, 2 and 3 (graph a,b and c respectively) with fitted Gamma distributions, determined by the circle-fitting method. (a) In Gel 1, the majority of the pores are larger than 100 nm, and the largest detected pore is  $1.0 \mu\text{m}$ . Gamma parameters were:  $\alpha = 2.38962$ ,  $\beta = 129.132$ . (b) In Gel 2, a minority of the pores were larger than 100 nm. Gamma parameters were:  $\alpha = 2.56869$ ,  $\beta = 22.4094$ . (c) In Gel 3, all pores were smaller than 100 nm. Gamma parameters were:  $\alpha = 1.75853$ ,  $\beta = 10.249$ . (d) An overlay of the gamma distributions, for comparison.

larger and inkbottle-shaped connecting features, is important information that cannot be extracted from the 2D projected images. If the mentioned structures are present in our materials, this could also be a part of the explanation of the results. Based on this discussion, retrieving actual 3D data of the porous silica sample was a natural continuation of the research.

### 3.4 Estimation of mass thickness of embedded aggregated silica nanospheres

The log-likelihood approach was evaluated as a tool for getting information in the third dimension from 2D STEM images. Here, the intensity response from a silica nanoparticle gel (Bindzil 40/130, 9.0 wt%, 0.9 M NaCl, pH=7.8) HAADF-STEM micrograph as a function of silica mass thickness was studied. Using this approach, a simulated micrograph could be reconstructed from the original one.

- First, a simulated micrograph was generated to resemble the characteristic appearance of an actual HAADF-STEM micrograph.
- Using this simulated micrograph as reference, the log-likelihood approach was used for recreating the simulated micrograph. The recreated image and the originally simulated micrograph was compared, and the resemblance was almost perfectly accurate. The conclusion of this comparison is that the log-likelihood is a good enough approach to try on an actual micrograph.
- The log-likelihood approach was therefore used for recreating an image of an actual HAADF-STEM micrograph. The original and the recreated image were compared, and the resemblance was good. (However, due to difficulties in computationally resolving the more intense areas of the micrograph, the resemblance is less than in the former case.)

The intensity could be described as a power function of the mass thickness for each point in the plane. This description was proven to be significantly better than describing the relationship linearly.

In the histogram of the log-likelihood reconstructed image of the micrograph, intensity maxima for one and two discs blocking the electron beam path could be distinguished. In the (2D) histogram of the actual micrograph, no significantly distinguished peaks for the particles could be seen. This is most likely caused by the fact that the micrograph shows projections of spherical particles, which can overlap in any angle related to the electron beam. Hence, there will not likely be clearly distinguishable intensity peaks. However, since it was proven that the log-likelihood approach works flawlessly if the sample contains discs oriented perpendicularly to the electron beam instead of spheres, it is possible to estimate the 3D structure from an actual 2D HAADF-STEM micrograph via this approach. The 3D information in this

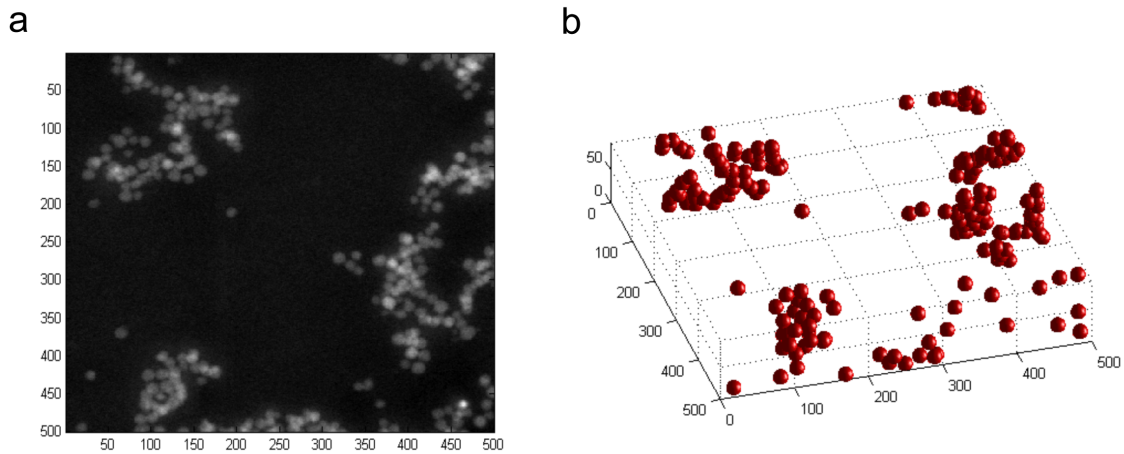


**Figure 3.7:** (a) A HAADF-STEM image acquired from a 90 nm thick specimen of a gel of Bindzil 40/130 particles. (b) A simulated 3D structure from the HAADF-STEM image, constructed using intensity based mass thickness estimation. Image courtesy of Matias Nordin.

simulated image can be used to recreate (non-unique) 3D structures corresponding to the original micrograph - an important step toward the creation of larger simulated 3D structures, and also important for statistical gelation studies[73], see figure 3.7.

### 3.5 Ongoing study: 3D imaging of nanostructured silica gels

As a natural step following the results described above, next focus is on extracting the 3D structure of the material on the nanoscale. The purpose is to investigate the direct connection between pore size and mass transport for different nanoporous silica gels, in 3D. One of the scientific challenges here is to get quantitative structural data in 3D[60].

Using 3D STEM, the 3D PSDs can be analysed. Both the reconstructed 3D structure and the PSDs are important input for flow and diffusion simulations within the porous material. We used our reconstructed 3D structure as a template for Lattice-Boltzmann (LB) water transport simulations for both flow and diffusion. LB modelling is a powerful tool in fluid dynamic simulations[74].

For the visualisation of the gels, the software Avizo 9 was used. The particle threshold was set manually, by visually comparing the OrthoSlices (data slices from the SIRT reconstruction) to the isosurface, while adjusting the isosurface threshold. Pixels with intensity values above the particle threshold are interpreted as silica, and pixels with intensity values below it are interpreted as resin (background). For Gel 1, the thresholding was done directly. For Gel 2, two filtering steps were needed

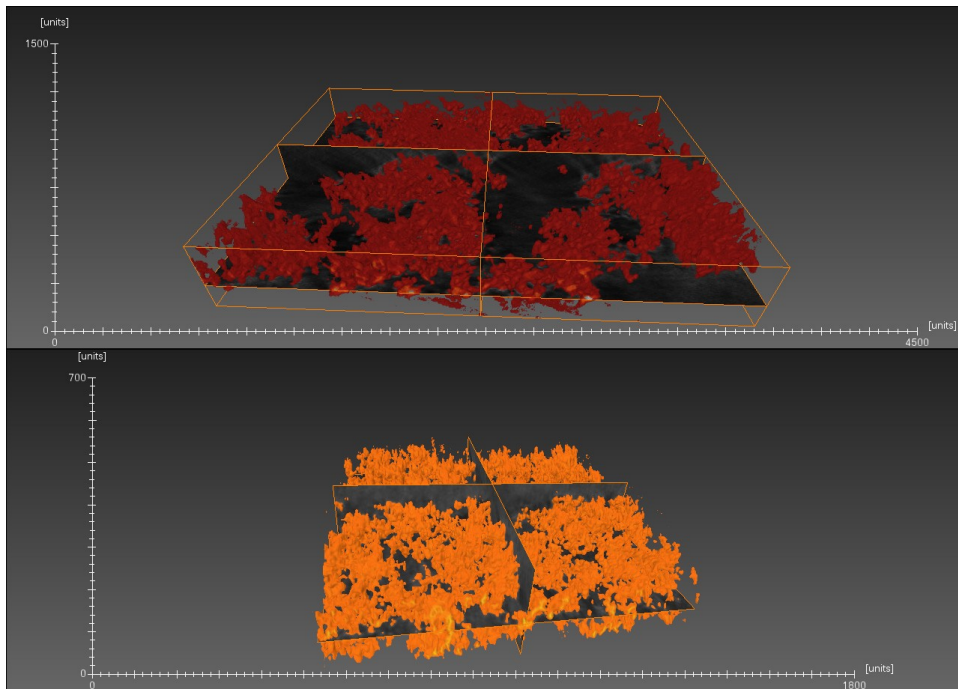


**Figure 3.8:** Visualisations of 3D reconstructions of Gel 1 (particles in red) and Gel 2 (particles in orange), displaying the volume rendering and slices through the structure in all directions (OrthoSlices). The software Avizo 9 (Visualization Sciences Group, an FEI Company) was used for the filtering and visualisation. One unit length represents one nanometer.

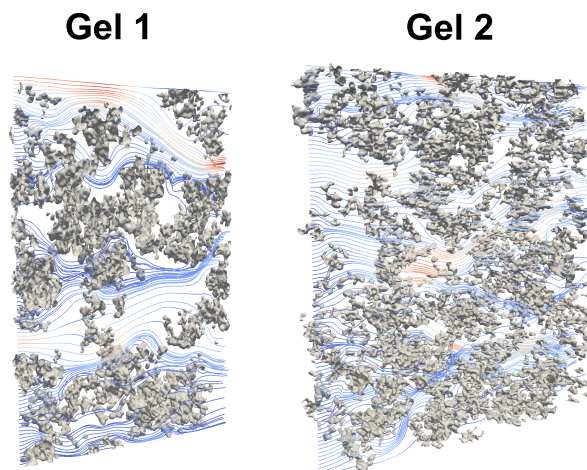


**Figure 3.9:** Lattice-Boltzmann simulations of water flow through the reconstructed 3D volumes of Gel 1 and 2, displaying the flow lines through the structure in one direction. Image courtesy of Tobias Gebäck.

in order to remove noise while preserving the particle edges: an edge-preserving smoothing step and a Gaussian 3D filter

The results of the 3D reconstructions are visualised in figure 3.8. The obtained structure data are quantitative in the directions perpendicular to the electron beam, but not in the direction parallel to the beam, due to the missing wedge effect. A possible approach to obtain quantitative data in all directions could be to incorporate a pillar shaped sample structure[75] or use more sophisticated reconstruction algorithms using prior knowledge[60].

The visualisation of the flow lines in the LB simulation of the flow is shown in figure 3.9. Flow simulations with this high magnification will, as the work continues, be complemented with simulations through structures imaged with lower magnification, in order for the permeability to be representative for the whole sample. Diffusion simulations however, are representative even at this higher magnification.

The LB simulations in the 3D reconstructions could, if this is the case, confirm that at the length scale of Gel 2 and 3, flow is completely indifferent to the PSD. In order to determine if this is the case, high magnification 3D reconstructions on Gel 3, as well as lower magnification 3D reconstructions of all three samples need to be done.

By this study, we provide further insight on when 3D imaging is crucial for understanding mass transport, and when 2D imaging provides sufficient information. Another interesting aspect is how large the 3D structures need to be in order for the LB simulations to provide a thorough understanding of the correlation between detailed nanostructure and mass transport.



## Chapter 4

# Summary of included papers

In this section, the methods and main conclusions of the included papers are summarised.

### 4.1 Paper I

The study presented in **Paper I** was performed in collaboration with the chemical and biological engineering, and mathematics departments at Chalmers, as well as SP Food and Bioscience (former known as SIK). Here, three different porous silica gels were characterised in 2D. Their mass transport properties were tested using two common techniques: gravitationally driven steady state flow and NMR diffusometry. The structural characterisation of the gels was performed by analysing the 2D micrographs.

The article provides new insight in mass transport on the nanoscale. Two of the three investigated samples had near identical convective flow data, despite a clear structural difference. This contradiction is something that needs to be investigated further in order to fully understand how the nanostructure of a porous material affects the mass transport. The explanation for the difference in flow properties is likely to be found in the 3D structure of these gels.

### 4.2 Paper II

This paper evaluates a mass thickness response estimation from HAADF-STEM images of embedded silica nanoparticle gel samples. The research was conducted as a part of the creation of a soft materials characterisation toolbox.

Here, silica mass thickness was estimated from a STEM micrograph, using the prior knowledge that the gel is composed of nanospheres. Using a statistical approach to the problem of making deductions of the third dimension from 2D micrographs, the intensity profiles of the micrographs was used as an indicator of the 3D structure. It was shown that the mass-thickness response could be fitted to a power law.

Using the results from this paper, it is possible to obtain a 3D reconstruction from just one 2D image. This reconstruction will however not be a unique solution, but it is still valuable for e.g. statistical gel aggregation studies and for creating larger 3D structures to be used in computer simulations of flow and diffusion. The article provides fundamental understanding of why actual 3D imaging is so important, especially as a validation step for more statistical methods by which larger structures can be simulated.

## Chapter 5

# Summary of work

This work has focused on gaining knowledge on the direct connection between the detailed material nanostructure and mass transport properties of soft porous materials. The combination of TEM tomography and advanced preparation techniques for high-resolution microscopy provides unique structure information for understanding structure-transport relationships. The soft porous material used was silica nanoparticle gels with different pore sizes. The porosity length scale of the silica gel samples was chosen to reflect a length scale where the exact influence of flow versus diffusion is experimentally unknown. We used 2D imaging and 3D STEM to characterise three different colloidal silica nanoparticle gels concerning the primary particle size and morphology, VWMV of pores, as well as PSDs. The data were compared to the mass transport data on both flow and diffusion. The nanoscale experimental data were also used for quantitative statistical modelling of the material structure in two dimensions, using the log-likelihood method.

An important part of the project was to continuously work on improving the resolution in the 3D reconstructions. Important parameters to enhance are micrograph contrast, handling the MW and aligning the images in the tilt series to perfection.

One unique aspect of the study is that the reconstructed 3D nanoscale structure has been used for LB mass transport simulations. This provides opportunities of comparing mass transport properties and mass transport flow simulations through the soft porous materials. Simulating mass transport through the reconstructed structure provides an important step towards understanding mass transport in porous nanoscale materials. A valuable complement to these simulations can be simulations in structures where the whole material structure has been produced by computer simulation.

## 5.1 Conclusions

The building blocks of the silica gels were characterised based on TEM images for the first time. It was confirmed that Bindzil 40/130 had spherical particles, and it was concluded that Bindzil XP1 and GB3000 had different degree of structure

complexity and large variations. It was experimentally concluded that for the silica gels with a VWMV of approximately 120 nm and less, the water transport is very low and seems to be independent of pore size.

The statistical approach to the problem of making deductions of the third dimension from 2D micrographs, showed that using the intensity profiles of the micrographs as an indicator of the 3D structure is useful if it is possible to validate it with a 3D reconstruction of the structure.

From the ongoing 3D STEM study, we show that 3D imaging of the silica networks is possible. The information can be directly used for water transport simulations, that are more accurate compared to the experimental data the more representative the imaged sample is to the whole structure. The characterisation of the PSDs could now be performed in 3D.

## 5.2 Outlook

For future 3D investigations, it would be interesting to use rod like samples in order to avoid the MW artefact, due to increasing sample thickness. Unfortunately, this approach is not straight forward for soft materials and there are some obstacles to get past in order to have a working acquisition method for rod shaped or needle like samples. An alternative way to circumvent the MW artefact is to use an iterative reconstruction technique based on prior knowledge. In our case, an algorithm addressing porous samples would be especially beneficial.

The information obtained by studying silica nanoparticle gels can also be useful concerning other soft porous materials where mass transport is important.

# Acknowledgements

I take this opportunity to express my appreciation to several persons who contributed in various ways to this work and to the writing of this licentiate thesis.

I acknowledge my main supervisor and group leader Eva Olsson for providing support and guidance concerning the wider perspective, as well as the finer details of science and scientific communication. I would also like to thank my former main supervisor Anne-Marie Hermansson, and my co-supervisors Niklas Lorén and Stefan Gustafsson, and my mentor Annika Altskär for helping me with everything from research questions to technical writing. All your help has been extremely valuable to me.

Thank you Mikael Persson at AkzoNobel PPC AB, for all your help regarding the properties and applications of silica, for answering all my questions, for providing me with sample material and for taking interest in my work.

Tobias Gebäck, Henrike Häbel, Christoffer Abrahamsson, Matias Nordin, Aila Särkkä, and Mats Rudemo: Thank you for great collaboration and scientific contributions, for answering all my questions about your individual areas of expertise, and for taking interest in my work.

I also acknowledge Dr. Hamed Heidari and Prof. Sara Bals in the Electron microscopy for materials science (EMAT) group at the University of Antwerp, and Dr. Zineb Saghi and Prof. Paul Midgley in the Electron microscopy group at the University of Cambridge: Thank you all for sharing your expertise and providing valuable input on both 3D imaging of nanomaterials, and their reconstruction.

A great thank you to Anders Kvist, Ola Löfgren and the rest of the Chalmers Materials Analysis Laboratory group, for your never-ending patience and help regarding the instruments and computers, both when the reason for trouble is unknown and when it was not.

I thank all my past and present colleagues in the Eva Olsson group, the Materials Microstructure group and the former Microscopy and Microanalysis group at the Department of Applied Physics. Thank you also to all the past and present colleagues of the Structure and Materials Design department at SP Food and Bioscience, former SIK. A special thanks also to my occasional officemate Wolfgang Jäger for your frequent words of encouragement, and to my former officemate Markus Löffler for raising my spirit!

I thank the SuMo Biomaterials collaboration for providing a stimulating research environment, and I thank all my colleagues within the collaboration, both from

academia and industry. I also express my gratitude to VINNOVA and the Swedish foundation for strategic research (SSF), for funding my research project, and the ESTEEM2 collaboration for providing connections within all of Europe.

A special thank you to Mattias Goksör, Anna-Karin Gustavsson, och Caroline B. Adiels, in the Biophotonics group at Göteborg University. Thank you for still making me feel right at home in your group, and for your ever-lasting support, encouragement and friendship.

Thank you to my parents Annette and Per Hamngren for encouraging me, and to my brother Daniel Hamngren for letting me disturb you with the most difficult binarisation problems, amongst other things.

Last but not least, I would like to pay very special appreciations to my husband Peter Blomqvist, without whom's endless support I could never manage. Thank you for always encouraging me, even when I am stressed out and self-conscious. I cannot wait to begin our future adventures as a family of three!

Göteborg, 18th March 2015  
*Charlotte Hamngren Blomqvist*





# Bibliography

- [1] P.-G. DE GENNES. Soft Matter. Nobel Lecture: [http://www.nobelprize.org/nobel\\_prizes/physics/laureates/1991/gennes-lecture.pdf](http://www.nobelprize.org/nobel_prizes/physics/laureates/1991/gennes-lecture.pdf) (1991). Accessed March 13, 2015.
- [2] R. A. L. JONES, *Soft Condensed Matter*, Oxford University Press Inc., New York, NY, USA (2002).
- [3] ROYAL SOCIETY OF CHEMISTRY. About Soft Matter. <http://www.rsc.org/publishing/journals/sm/about.asp>. Accessed March 30, 2014.
- [4] A.-M. HERMANSSON, N. LORÉN, AND M. NYDÉN, The importance of microstructure for solvent and solute diffusion on the micro and nano length scales, In P. Buera, J. Welti-Chanes, P. Lillford, and H. Corti, editors, *Water properties of Food, Pharmaceuticals and Biological Materials*, CRC Taylor and Francis, Boca Raton, FL (2006).
- [5] I. NISCHANG, Porous polymer monoliths: Morphology, porous properties, polymer nanoscale gel structure and their impact on chromatographic performance, *Journal of Chromatography A* **1287**, 39–58 (2013).
- [6] Z. Y. YUAN AND B. L. SU, Insights into hierarchically meso-macroporous structured materials, *Journal of Materials Chemistry* **16**, 663–677 (2006).
- [7] F. ZAERA, Nanostructured materials for applications in heterogeneous catalysis, *Chemical Society Reviews* **42**, 2746–2762 (2013).
- [8] D. W. H. LAMBERT, P. H. J. GREENWOOD, AND M. C. REED, Advances in gelled-electrolyte technology for valve-regulated lead-acid batteries, *Journal of power sources* **107**, 173–179 (2002).
- [9] A.-M. HERMANSSON, Water- and Fatholding, In J. R. Mitchell and D. A. Ledward, editors, *Functional properties of food macromolecules*, pages 273–314, Elsevier Inc., Waltham, MA (1986).
- [10] J. ROUQUEROL, D. AVNIR, C. W. FAIRBRIDGE, D. H. EVERETT, J. H. HAYNES, N. PERNICONE, J. D. F. RAMSAY, K. S. W. SING, AND K. K.

- UNGER, Recommendations for the characterization of porous solids, *Pure and Applied Chemistry* **66**, 1739–1758 (1994).
- [11] P. A. C. GANE, C. J. RIDGWAY, E. LEHTINEN, R. VALIULLIN, I. FURO, J. SCHOELKOPF, H. PAULAPURO, AND J. DAICIC, Comparison of NMR cryoporometry, mercury intrusion porosimetry, and DSC thermoporosimetry in characterizing pore size distributions of compressed finely ground calcium carbonate structures, *Industrial & Engineering Chemistry Research* **43**, 7920–7927 (2004).
- [12] A. GUEVEN AND Z. HICSASMAZ, *Pore Structure in Food: Simulation, Measurement and Applications*, volume VIII, Springer, cop., New York, USA; London, UK (2013).
- [13] S. JAGANATHAN, H. V. TAFRESHI, AND B. PPURDEYHIMI, Modeling liquid porosimetry in modeled and imaged 3-D fibrous microstructures, *Journal of Colloid and Interface Science* **326**, 166–175 (2008).
- [14] M. THOMMES AND K. A. CYCHOSZ, Physical adsorption characterization of nanoporous materials: progress and challenges, *Adsorption-Journal of the International Adsorption Society* **20**, 233–250 (2014).
- [15] R. SCHMIDT, E. W. HANSEN, M. STOCKER, D. AKPORIAYE, AND O. H. ELLESTAD, Pore-size determination of MCM-41 mesoporous materials by means of H-1-NMR spectroscopy, N-2 adsorption, and HREM - a preliminary-study, *Journal of the American Chemical Society* **117**, 4049–4056 (1995).
- [16] K. ISHIKIRIYAMA, M. TODOKI, AND K. MOTOMURA, Pore-size distribution (PSD) measurements of silica-gels by means of differential scanning calorimetry .1. Optimization for determination of PSD, *Journal of Colloid and Interface Science* **171**, 92–102 (1995).
- [17] K. ISHIKIRIYAMA AND M. TODOKI, Pore-size distribution (PSD) measurements of silica-gels by means of differential scanning calorimetry .2. Thermoporosimetry, *Journal of Colloid and Interface Science* **171**, 103–111 (1995).
- [18] J. J. HOWARD AND W. E. KENYON, Determination of pore-size distribution in sedimentary-rocks by proton nuclear-magnetic-resonance, *Marine and Petroleum Geology* **9**, 139–145 (1992).
- [19] N. LORÉN, L. SHTYKOVA, S. KIDMAN, P. JARVOLL, M. NYDÉN, AND A.-M. HERMANSSON, Dendrimer Diffusion in kappa-Carrageenan Gel Structures, *Biomacromolecules* **10**, 275–284 (2009).

- [20] B. WALTHER, N. LORÉN, M. NYDÉN, AND A.-M. HERMANSSON, Influence of kappa-carrageenan gel structures on the diffusion of probe molecules determined by transmission electron microscopy and NMR diffusometry, *Langmuir* **22**, 8221–8228 (2006).
- [21] N. LORÉN, H. HAGSLATT, M. NYDÉN, AND A.-M. HERMANSSON, Water mobility in heterogeneous emulsions determined by a new combination of confocal laser scanning microscopy, image analysis, nuclear magnetic resonance diffusometry, and finite element method simulation, *Journal of Chemical Physics* **122** (2005).
- [22] A.-M. HERMANSSON AND M. LUCISANO, Gel characteristics - waterbinding properties of blood-plasma gels and methodological aspects on the waterbinding of gel systems, *Journal of Food Science* **47**, 1955–1959 (1982).
- [23] A.-M. HERMANSSON, Gel characteristics - compression and penetration of blood-plasma gels, *Journal of Food Science* **47**, 1960–1964 (1982).
- [24] A.-M. HERMANSSON, Gel characteristics - structure as related to texture and waterbinding of blood-plasma gels, *Journal of Food Science* **47**, 1965–1972 (1982).
- [25] K. SOTT, T. GEBÄCK, M. PIHL, N. LORÉN, A. M. HERMANSSON, A. HEINTZ, AND A. RASMUSON, Micro-PIV methodology using model systems for flow studies in heterogeneous biopolymer gel microstructures, *Journal of Colloid and Interface Science* **398**, 262–269 (2013).
- [26] C. ABRAHAMSSON, L. NORDSTIERNA, J. BERGENHOLTZ, A. ALTSKÄR, AND M. NYDÉN, Magnetically induced structural anisotropy in binary colloidal gels and its effect on diffusion and pressure driven permeability, *Soft Matter* **10**, 4403 – 4412 (2014).
- [27] S. WASSEN, R. BORDES, T. GEBAECK, D. BERNIN, E. SCHUSTER, N. LOREN, AND A.-M. HERMANSSON, Probe diffusion in phase-separated bicontinuous biopolymer gels, *Soft Matter* **10**, 8276–8287 (2014).
- [28] E. SCHUSTER, J. ECKARDT, A.-M. HERMANSSON, A. LARSSON, N. LOREN, A. ALTSKAR, AND A. STROM, Microstructural, mechanical and mass transport properties of isotropic and capillary alginate gels, *Soft Matter* **10**, 357–366 (2014).
- [29] P. NELSON, *Biological physics - Energy, Information, Life*, W. H. Freeman and Company, New York, NY, USA, updated first edition (2008).
- [30] D. J. BEEBE, G. A. MENSING, AND G. M. WALKER, Physics and applications of microfluidics in biology, *Annual Review of Biomedical Engineering* **4**, 261–286 (2002).

- [31] L. MASARO AND X. X. ZHU, Physical models of diffusion for polymer solutions, gels and solids, *Progress in polymer science* **24**, 731–775 (1999).
- [32] R. K. ILER, *The Chemistry of Silica - Solubility, Polymerization, Colloid and Surface Properties, and Biochemistry*, John Wiley and Sons, Inc., Hoboken, NJ, USA (1979).
- [33] H. WU, J.-J. XIE, AND M. MORBIDELLI, Kinetics of colloidal gelation and scaling of the gelation point, *Soft Matter* **9**, 4437–4443 (2013).
- [34] AKZONOBEL PPC AB. Ground Consolidation: Building with stability. [https://www.akzonobel.com/colloidalsilica/application/ground\\_consolidation/index.aspx](https://www.akzonobel.com/colloidalsilica/application/ground_consolidation/index.aspx). Accessed March 27, 2014.
- [35] M. R. NOLL, C. BARTLETT, AND T. M. DOCHAT, In Situ permeability reduction and chemical fixation using colloidal silica, Sixth National Outdoor Action Conference on Aquifer Restoration, sponsored by National Ground Water Assn., Las Vegas, NV (1992).
- [36] AKZONOBEL PPC AB. Bindzil GB for lead-acid batteries. Booklet (2011).
- [37] T. SUGAR AND F. CUBA, An Electron Microscope Study of the Structure of Silica Gels, In R. Ross, editor, *Proc. of the Third International Conference on Electron Microscopy, London 1954*, pages 530–532, Royal Microscopical Society (1956).
- [38] X. J. CAO, H. Z. CUMMINS, AND J. F. MORRIS, Structural and rheological evolution of silica nanoparticle gels, *Soft Matter* **6**, 5425–5433 (2010).
- [39] A. SCHANTZ ZACKRISSON, A. MARTINELLI, A. MATIC, AND J. BERGENHOLTZ, Concentration effects on irreversible colloid cluster aggregation and gelation of silica dispersions, *Journal of colloid and interface science* **301**, 137–144 (2006).
- [40] A. SCHANTZ ZACKRISSON, J. S. PEDERSEN, AND J. BERGENHOLTZ, A small-angle X-ray scattering study of aggregation and gelation of colloidal silica, *Colloids and surfaces A - physicochemical and engineering aspects* **315**, 23–30 (2008).
- [41] M. PERSSON. Private communication (2014). AkzoNobel, PPC AB.
- [42] G. MIE, Beiträge zur Optik trüber Medien, speziell kolloidaler Metallösungen, *Annalen der Physik* **330**, 377–445 (1908).
- [43] H. B. WEN, J. MORADIAN-OLDAK, W. LEUNG, P. BRINGAS, AND A. G. FINCHAM, Microstructures of an amelogenin gel matrix, *Journal of Structural Biology* **126**, 42–51 (1999).

- [44] A. R. SPURR, A low-viscosity epoxy resin embedding medium for electron microscopy, *Journal of ultrastructure research* **26**, 31–43 (1969).
- [45] J. AYACHE, *Sample preparation handbook for transmission electron microscopy: methodology*, Springer, cop., New York, USA; London, UK, 1st edition (2010).
- [46] A. CAVALIER, D. SPEHNER, AND B. M. HUMBEL, *Handbook of Cryo-Preparation Methods for Electron Microscopy*, CRC Press, Boca Raton, FL, USA (2009).
- [47] D. B. WILLIAMS AND B. C. CARTER, *Transmission electron microscopy : a textbook for materials science*, Springer, cop., New York, USA; London, UK, 2nd edition (2009).
- [48] J. FRANK, *Electron Tomography: Methods for Three-Dimensional Visualization of Structures in the Cell*, Springer, cop., New York, USA; London, UK (2006).
- [49] A. J. KOSTER, H. CHEN, J. W. SEDAT, AND D. A. AGARD, Automated microscopy and microscopy for electron tomography, *Ultramicroscopy* **46**, 207–227 (1992).
- [50] P. A. MIDGLEY, M. WEYLAND, J. M. THOMAS, AND B. F. G. JOHNSON, Z-Contrast tomography: a technique in three-dimensional nanostructural analysis based on Rutherford scattering, *Chemical communications* pages 907–908 (2001).
- [51] P. A. MIDGLEY AND M. WEYLAND, 3D electron microscopy in the physical sciences: the development of Z-contrast and EFTEM tomography, *Ultramicroscopy* **96**, 413–431 (2003).
- [52] A. KLUG AND J. T. FINCH, Structure of viruses of papilloma-polyoma type .I. Human wart virus, *Journal of molecular biology* **11**, 403–423 (1965).
- [53] W. O. SAXTON, W. BAUMEISTER, AND M. HAHN, 3-dimensional reconstruction of imperfect two-dimensional crystals, *Ultramicroscopy* **13**, 57–70 (1984).
- [54] J. RADON, On the determination of functions from their integrals along certain manifolds, *Berichte uber die Verhandlungen der Koniglich Sachsische Gesellschaft der Wissenschaften zu Leipzig, Mathematisch-Physikalische (translated)* **69**, 262–277 (1917).
- [55] J. R. KREMER, D. MASTRONARDE, AND J. MCINTOSH, Computer visualization of three-dimensional image data using IMOD, *Journal of Structural Biology* **116**, 71–76 (1996).

- [56] P. W. HAWKES, The electron microscope as a structure projector, In J. Frank, editor, *Electron Tomography: Methods for Three-Dimensional Visualization of Structures in the Cell*, pages 83–112, Springer (2006).
- [57] P. GILBERT, Iterative methods for 3-dimensional reconstruction of an object from projections, *Journal of theoretical biology* **36**, 105–117 (1972).
- [58] Z. SAGHI, D. J. HOLLAND, R. LEARY, A. FALQUI, G. BERTONI, A. J. SEDERMAN, L. F. GLADDEN, AND P. A. MIDGLEY, Three-Dimensional Morphology of Iron Oxide Nanoparticles with Reactive Concave Surfaces. A Compressed Sensing-Electron Tomography (CS-ET) Approach, *Nano letters* **11**, 4666–4673 (2011).
- [59] K. J. BATENBURG, S. BALS, J. SIJBERS, C. KUEBEL, P. A. MIDGLEY, J. C. HERNANDEZ, U. KAISER, E. R. ENCINA, E. A. CORONADO, AND G. VAN TENDELOO, 3D imaging of nanomaterials by discrete tomography, *Ultramicroscopy* **109**, 730–740 (2009).
- [60] G. VAN EYNDHOVEN, M. KURTTEPELI, C. J. VAN OERS, P. COOL, S. BALS, K. J. BATENBURG, AND J. SIJBERS, Pore REconstruction and Segmentation (PORES) method for improved porosity quantification of nanoporous materials, *Ultramicroscopy* **148**, 10–19 JAN 2015.
- [61] P. K. LUTHER, Sample shrinkage and radiation damage of plastic sections, In J. Frank, editor, *Electron Tomography: Methods for Three-Dimensional Visualization of Structures in the Cell*, pages 17–48, Springer (2006).
- [62] J. C. RUSS, *Image analysis of food microstructure*, CRC Press LLC, Boca Raton, FL, USA (2005).
- [63] V. BRUSASCO AND A. T. DINH-XUAN, Stereology: a bridge to a better understanding of lung structure and function, *European respiratory journal* **35**, 477–478 (2010).
- [64] H. GUNDERSEN, T. BENDTSEN, L. KORBO, N. MARCUSSEN, A. MOLLER, K. NIELSEN, J. NYENGAARD, B. PAKKENBERG, F. SORENSEN, A. VESTERBY, AND M. WEST, Some New, Simple and Efficient Stereological Methods and their Use in Pathological Research and Diagnosis - Review Article, *APMIS* **96**, 379–394 (1988).
- [65] H. J. G. GUNDERSEN, P. BAGGER, T. F. BENDTSEN, S. M. EVANS, L. KORBO, N. MARCUSSEN, A. MOLLER, K. NIELSEN, J. R. NYENGAARD, B. PAKKENBERG, F. B. SORENSEN, A. VESTERBY, AND M. J. WEST, The New Stereological Tools - Disector, Fractionator, Nucleator and Point Sampled Intercepts and their Use in Pathological Research and Diagnosis, *APMIS* **96**, 857–881 (1988).

- [66] N. LORÉN, M. LANGTON, AND A.-M. HERMANSSON, Confocal Laser Scanning Microscopy and Image Analysis of Kinetically Trapped Phase-Separated Gelatin/Maltodextrin Gels, *Food Hydrocolloids* **13**, 185–198 (1999).
- [67] P. MOUTON, *Principles and Practices of Unbiased Stereology - An Introduction for Bioscientists*, The John Hopkins University Press, Baltimore, MA, USA (2002).
- [68] H. J. G. GUNDERSEN AND E. B. JENSEN, Stereological Estimation of the Volume-Weighted Mean Volume of Arbitrary Particles Observed on Random Sections, *Journal of Microscopy-Oxford* **138**, 127–142 (1985).
- [69] H. HÄBEL. Private communication (March, 2015). Chalmers University of Technology and University of Gothenburg, Department of Mathematical Sciences.
- [70] F. TAVENAS, P. JEAN, P. LEBLOND, AND S. LEROUEIL, The permeability of natural soft clays .2. Permeability characteristics, *Canadian Geotechnical Journal* **20**, 645–660 (1983).
- [71] W. S. PRICE, *Pulsed-Field Gradient Nuclear Magnetic Resonance as a Tool for Studying Translational Diffusion: Part 1. Basic Theory*, John Wiley & Sons, Inc., Hoboken, NJ (1997).
- [72] S. BABU, J. C. GIMEL, AND T. NICOLAI, Tracer diffusion in colloidal gels, *Journal of Physical Chemistry B* **112**, 743–748 (2008).
- [73] H. HÄBEL, A. SÄRKKÄ, M. RUDEMO, C. HAMNGREN BLOMQUIST, E. OLSSON, C. ABRAHAMSSON, AND M. NORDIN, From static micrographs to particle aggregation dynamics in three dimensions (In manuscript).
- [74] M. C. SUKOP AND D. T. THORNE, *Lattice Boltzmann Modeling An Introduction for Geoscientists and Engineers*, Springer, cop., New York, USA; London, UK, 2nd edition (2006).
- [75] N. KAWASE, M. KATO, H. NISHIOKA, AND H. JINNAI, Transmission electron microtomography without the "missing wedge" for quantitative structural analysis, *Ultramicroscopy* **107**, 8–15 JAN 2007.

